Published for SISSA by Springer

Received: December 8, 2018
Revised: March 17, 2019
Accepted: April 15, 2019
Published: April 29, 2019

Determination of α_s from static QCD potential: OPE with renormalon subtraction and lattice QCD

Hiromasa Takaura,[a,1] **Takashi Kaneko,**[b] **Yuichiro Kiyo**[c] **and Yukinari Sumino**[d]

[a] *Department of Physics, Kyushu University, Fukuoka, 819-0395 Japan*
[b] *Theory Center, KEK, Tsukuba, Ibaraki, 305-0801 Japan*
[c] *Department of Physics, Juntendo University, Inzai, 270-1695, Japan*
[d] *Department of Physics, Tohoku University, Sendai, 980-8578 Japan*

E-mail: takaura@phys.kyushu-u.ac.jp, ykiyo@juntendo.ac.jp, takashi.kaneko@kek.jp, sumino@tuhep.phys.tohoku.ac.jp

Abstract: We determine the strong coupling constant α_s from the static QCD potential by matching a theoretical calculation with a lattice QCD computation. We employ a new theoretical formulation based on the operator product expansion, in which renormalons are subtracted from the leading Wilson coefficient. We remove not only the leading renormalon uncertainty of $\mathcal{O}(\Lambda_{\rm QCD})$ but also the first r-dependent uncertainty of $\mathcal{O}(\Lambda_{\rm QCD}^3 r^2)$. The theoretical prediction for the potential turns out to be valid at the static color charge distance $\Lambda_{\overline{\rm MS}} r \lesssim 0.8$ ($r \lesssim 0.4\,\text{fm}$), which is significantly larger than ordinary perturbation theory. With lattice data down to $\Lambda_{\overline{\rm MS}} r \sim 0.09$ ($r \sim 0.05\,\text{fm}$), we perform the matching in a wide region of r, which has been difficult in previous determinations of α_s from the potential. Our final result is $\alpha_s(M_Z^2) = 0.1179^{+0.0015}_{-0.0014}$ with 1.3% accuracy. The dominant uncertainty comes from higher order corrections to the perturbative prediction and can be straightforwardly reduced by simulating finer lattices.

Keywords: QCD Phenomenology, Lattice field theory simulation

ArXiv ePrint: 1808.01643

[1] Corresponding author.

Open Access, © The Authors.
Article funded by SCOAP[3].

https://doi.org/10.1007/JHEP04(2019)155

Contents

1 Introduction 1

2 Theoretical framework 4
- 2.1 Formula to subtract renormalons 5
- 2.2 Treatment of US scale 8
- 2.3 Higher order perturbative uncertainty 10

3 α_s determination 11
- 3.1 Lattice simulations 11
- 3.2 Analysis (I): two-step analysis 12
  - 3.2.1 Continuum extrapolation 12
  - 3.2.2 Consistency checks and comparison with conventional methods 15
  - 3.2.3 α_s determination: matching between OPE and lattice result 20
- 3.3 Analysis (II): global fit 23
- 3.4 Summary of results 28

4 Conclusions and discussion 29

A Coefficients of perturbative calculation 30

B Formulation to extract $V_S^{\mathrm{RF}}(r)$ from $V_S(r)$ 31

C Definition of $\Lambda_{\overline{\mathrm{MS}}}$ 33

D χ^2 and covariance matrix 33

E Case including data at $r = a$ in Analysis (I) 35

F Additional analyses on systematic errors 36

1 Introduction

Today, facing frontier experiments of particle physics, such as the ones at LHC and Super B Factory (Belle II), there exist increasing demands for more accurate theoretical predictions based on QCD on various phenomena of the strong interaction. Precise determination of the strong coupling constant α_s, which is a fundamental parameter of QCD, sets a benchmark for such predictions. In fact, many theoretical developments are required for improving accuracy of α_s determination, and once α_s is determined, it serves as an input parameter for various predictions. For instance, a precise value of α_s will play crucial roles

JHEP04(2019)155

in measurements of Higgs boson properties, in searches for new physics, or in high-precision flavor physics. It is also demanded in the context of precise determination of the top quark mass, predicting running of the Higgs quartic coupling, etc.

Let us quote the current value of α_s, given as the world-combined result by the Particle Data Group (PDG), $\alpha_s(M_Z^2) = 0.1181 \pm 0.0011$ [1]. Dominant contributions to this value come from determinations by lattice QCD, which have smaller errors than other determinations using more direct experimental inputs. The Flavor Lattice Averaging Group (FLAG) reports an average of lattice determinations as $\alpha_s(M_Z^2) = 0.1182 \pm 0.0012$ [2] based on the studies in refs. [3–7]. The relative accuracies of these current values are 0.9–1.0 per cent.

In determinations of α_s by lattice QCD, we need to pay attention to the so-called "window problem," as pointed out in the FLAG report [2]. This is a problem that it is difficult to find a wide enough region where both lattice QCD and perturbative QCD predictions are accurate. A lattice simulation is carried out with a finite lattice spacing a, whose inverse plays the role of an ultraviolet (UV) cutoff scale. Hence, the lattice results are accurate in the energy region $Q \ll a^{-1}$. On the other hand, perturbative calculations are accurate at $Q \gtrsim 1$ GeV($\gg \Lambda_{\rm QCD} \sim 300$ MeV). Determinations of α_s are performed by matching of both results. It turns out that, for currently available lattice cutoff scales, the energy window 1 GeV $\lesssim Q \ll a^{-1}$ cannot be taken widely.

The method of finite volume scheme combined with step-scaling [8–11] can resolve this problem even at currently available lattice cutoffs. In this method, discretization and finite volume effects are kept under control by a finite volume scheme, while lattice data after the step-scaling running can be matched with perturbation theory at sufficiently high scale. As a result, matching with perturbative prediction can be performed at 10–100 GeV. A recent determination based on this method gives $\alpha_s(M_Z^2)$ with 0.7 per cent relative accuracy [12] (not yet included in the above average values).

In this paper, we determine α_s by taking an alternative approach to the window problem: we enlarge the validity range of a theoretical calculation to lower energy where lattice calculations are accurate due to $Q \ll a^{-1}$. For this purpose, we use the operator product expansion (OPE) as a theoretical framework. Its difference from perturbative calculations can be stated as follows. Perturbative predictions have an inevitable uncertainty known as renormalon uncertainty, which stems from a certain divergent behavior of perturbative series at large orders. (See ref. [13] for a review of renormalon.) For a dimensionless observable $R(Q)$ with typical energy scale Q, a renormalon uncertainty is estimated as $\mathcal{O}((\Lambda_{\rm QCD}/Q)^n)$ with a positive integer n (dependent on the observable). In the context of the OPE of the same observable, given by

$$R(Q) = C_1(Q) + C_{\mathcal{O}_1}(Q)\frac{\langle 0|\mathcal{O}_1|0\rangle}{Q^n} + \dots , \tag{1.1}$$

the perturbative result is encoded in the leading Wilson coefficient C_1. In fact, the renormalon uncertainty of C_1 generally has the same order of magnitude as the leading nonperturbative effect (the second term), which corresponds to $\dim[\mathcal{O}_1] = n$ [14]. It is expected that the renormalon uncertainty in the leading Wilson coefficient gets canceled when the

JHEP04(2019)155

nonperturbative matrix element is added. Hence, the OPE may realize a wider validity range due to the absence of the renormalon uncertainty, in particular at lower energy side.

However, the OPE cannot be made a maximal use as long as we naively calculate C_1 in the ordinary perturbation theory. This is because we do not know sufficiently about the nonperturbative matrix element. It is not obvious how to practically eliminate the renormalon uncertainty of C_1 using the OPE. In the case where the renormalon uncertainty remains in C_1, one encounters a difficulty that the nonperturbative effect cannot be estimated using the OPE (1.1) since C_1 has an error comparable to this nonperturbative effect. In other words, a renormalon uncertainty causes a mixing between C_1 and the nonperturbative effect. Many studies considering the OPE in the literature are not free from such a difficulty.

In refs. [15, 16], a method to cope with a renormalon uncertainty has been proposed. This method enables us to divide C_1 into a renormalon uncertainty and a renormalon free part. By this, we remove a renormalon uncertainty from C_1 before referring to the nonperturbetive matrix element. In this method, we first define C_1 as a UV quantity à la Wilson by introducing an IR cutoff scale μ_f (corresponding to a factorization scale of an effective field theory). Then, we separate $C_1(Q^2;\mu_f)$ into its cutoff independent part and dependent part. While a cutoff dependent part exhibits a connection to the IR physics, a cutoff independent part is regarded as a genuine UV contribution. This cutoff independent part corresponds to a renormalon free part, determined within perturbation theory. Furthermore, by absorbing the cutoff dependent part into the leading nonperturbative matrix element, the nonperturbative matrix element can also be defined as a renormalon free quantity. Hence, we can define the leading Wilson coefficient and the leading nonperturbative effect such that they are clearly separated. This enables us to estimate the nonperturbative effect without being affected significantly from the higher order uncertainty of C_1.

We apply this calculation method for the static QCD potential following ref. [15]. The typical energy scale of the static QCD potential is r^{-1}, which is the inverse of the distance between the static color charges. The renormalons of the static QCD potential are located at half integers in the Borel u-plane. The first renormalon at $u = 1/2$ gives an $\mathcal{O}(\Lambda_{\rm QCD})$ uncertainty. This renormalon is known to be cancelled against twice the pole mass in the total energy once the pole mass is expressed in terms of a short-distance mass [17, 18]. (At this stage, the OPE in r is not necessary.) The next-to-leading renormalon at $u = 3/2$ gives the leading r-dependent uncertainty of $\mathcal{O}(\Lambda_{\rm QCD}^3 r^2)$. In the present work, we remove not only the $u = 1/2$ renormalon but also the $u = 3/2$ renormalon using the above renormalon subtraction in the OPE framework.

The OPE of the static QCD potential in r can be performed in the form of the multipole expansion within the effective field theory (EFT), potential non-relativistic QCD (pNRQCD) [19]. Thanks to this solid basis of pNRQCD, the $u = 3/2$ renormalon cancellation has been convincingly shown [19], which gives a solid basis to our OPE formula. We construct a renormalon subtracted Wilson coefficient (which will be denoted by $V_S^{\rm RF}$ below) based on the fixed order result, which is currently known up to the next-to-next-to-next-to-leading order ($\rm N^3LO$), i.e., $\mathcal{O}(\alpha_s^4)$ [20–23]. As mentioned, a unique feature of our renormalon subtraction is that not only the leading renormalon (at $u = 1/2$) but also the

JHEP04(2019)155

next-to-leading renormalon (at $u = 3/2$) is removed from $V_S^{\rm RF}$. In the OPE, the leading term is given by $V_S^{\rm RF} \sim \mathcal{O}(1/r)$. The NLO term represents the leading nonperturbative effect and is $\mathcal{O}(r^2)$. We include the NLO term with an unknown coefficient which is to be determined by a fit. We will explicitly show consistency with the OPE by comparing $V_S^{\rm RF}$ with a lattice result: the difference between them can be fitted by an $\mathcal{O}(r^2)$-term. Our OPE prediction turns out to be valid up to $\Lambda_{\rm QCD} r \lesssim 0.8$, corresponding to $r^{-1} \gtrsim 0.5$ GeV. This shows that our theoretical prediction indeed has a wider validity range than the ordinary perturbation theory, which is valid at $r^{-1} \gtrsim 1$ GeV.

We determine α_s from the static QCD potential by matching a lattice result with the above OPE where the renormalon uncertainty is subtracted. The lattice results that we use are obtained by the JLQCD collaboration at large cutoffs up to 4.5 GeV [24, 25], which facilitate the matching between lattice and the OPE calculations.

Determinations of α_s using the static QCD potential have been performed in ref. [7] with 3-flavor lattice simulation and in ref. [26] with 2-flavor lattice simulation. In these studies, perturbative calculations are matched with lattice results in the perturbative regime $\Lambda_{\rm QCD} r \lesssim 0.2$–$0.3$. Our determination is carried out with the OPE calculation, and the matching range is taken as $\Lambda_{\rm QCD} r \lesssim 0.6$–$0.8$. We have briefly reported our analysis in ref. [27].

This paper is organized as follows. In section 2, we present our theoretical formula to subtract renormalons in the OPE (partially supplemented in appendix B). In section 3, we determine α_s by matching the theoretical calculation with a lattice result. Lattice results and the way to determine α_s are also explained therein. Conclusions and discussion are given in section 4. Some referential materials and supplementary arguments are given in appendices.

2 Theoretical framework

Our renormalon subtraction formula [15] is constructed based on the EFT, potential nonrelativistic QCD (pNRQCD) [19]. This EFT factorizes two typical scales of the static QCD potential. One of the scales is the soft scale $\sim 1/r$, which is the inverse of the distance between the static color charges. The other is the ultrasoft (US) scale $\sim \Delta V (\ll 1/r)$, which is the energy difference between the octet and singlet bound states. pNRQCD enables us to investigate the US scale physics in a systematic expansion in $r\Delta V \ll 1$. The Lagrangian of this EFT consists of the singlet and octet matter fields and the US gluon fields, while the soft scale contributions are integrated out and encoded in the Wilson coefficients. Our formula is based on the multipole expansion, which expands the static QCD potential in r using the hierarchy $r\Delta V \ll 1$.

In section 2.1, we present our formula to subtract renormalons after a brief review of the multipole expansion, on which the formula is based. In section 2.2, we explain our treatment of the IR divergence in the three-loop result of the static QCD potential, which is related to the US scale dynamics. In section 2.3, we estimate the higher order perturbative uncertainty of the theoretical calculation, which is required in estimation of systematic errors in α_s determination.

JHEP04(2019)155

2.1 Formula to subtract renormalons

Our theoretical calculation is based on the multipole expansion, which gives an expansion of the static QCD potential in r [19]:

$$V_{\rm QCD}(r) = V_S(r) + \delta E_{\rm US}(r) + \dots \,. \tag{2.1}$$

The explicit r-dependence is given by $V_S \sim \mathcal{O}(1/r)$ and $\delta E_{\rm US} \sim \mathcal{O}(r^2)$. (The dots denote higher order terms in r.) The singlet potential V_S originates from the soft scale[1] $\sim 1/r$ ($\gg \Lambda_{\rm QCD}$) and can be evaluated in perturbation theory. In terms of the pNRQCD Lagrangian, V_S is a Wilson coefficient. Perturbative result in coordinate space is usually obtained through Fourier transform (FT) of the perturbative evaluation of $\alpha_V(q^2)$,

$$V_S(r) = -4\pi C_F \int \frac{d^3\vec{q}}{(2\pi)^3}\, e^{i\vec{q}\cdot\vec{r}} \frac{\alpha_V(q^2)}{q^2} \qquad (q = |\vec{q}|)\,, \tag{2.2}$$

where the perturbative result of $\alpha_V(q^2)$ is currently known up to three-loop order [21–23]:

$$\alpha_V(q^2) = \alpha_s(\mu^2) \sum_{n=0}^{3} [P_n(\log(\mu/q)) + \delta P_n(\log(\mu/q))] \left(\frac{\alpha_s(\mu^2)}{4\pi}\right)^n . \tag{2.3}$$

Here, P_n is an n-th order polynomial and we denote its constant part by a_n:

$$a_n = P_n(0) = P_n(\log(\mu/q))|_{\mu=q}\,. \tag{2.4}$$

The logarithmic terms in P_n can be calculated from the renormalization group (RG) equation and are expressed by a_k with $k < n$ and the coefficients of the beta function. δP_n represents the IR divergence and associated logarithmic dependence. It is zero for $n \le 2$, and non-zero for $n = 3$; see eq. (2.14) for δP_3. This IR divergence is different from renormalon uncertainties and its presence hardly affects the following renormalon subtraction formula. We explain our prescription for regularizing this divergence in the next section 2.2. We collect the explicit expressions for a_n in appendix A.

The NLO term of eq. (2.1), $\delta E_{\rm US}$, is dominantly determined by dynamics of the US scale $\sim \Delta V$. It is given by a correlator of the US fields in pNRQCD:

$$\delta E_{\rm US}(r) = -i\frac{2\pi\alpha_s}{3} \int_0^\infty dt\, e^{-i\Delta V t} \langle 0|\vec{r}\cdot\vec{E}^a(t)\varphi_{\rm adj}(t;0)^{ab}\vec{r}\cdot\vec{E}^b(0)|0\rangle\ , \tag{2.5}$$

where $\vec{E}^a$ is the US chromoelectric field; see ref. [19] for details.

Despite the fact that conceptually the singlet potential is a soft quantity, the integration region is usually taken as $0 \le q < \infty$ as shown in eq. (2.2). In particular, IR region of the integral is known to cause renormalon uncertainties in V_S, and it brings about a mixing between V_S and $\delta E_{\rm US}$. To avoid this feature, we construct V_S as a renormalon free quantity below, following ref. [15].

[1] In the pNRQCD terminology, the "soft scale" corresponds to the UV scale, which has been integrated out.

JHEP04(2019)155

We first introduce a factorization (cutoff) scale μ_f to divide the energy region as $\Lambda_{\rm QCD} \ll \mu_f \ll 1/r$, and define V_S as a soft quantity in terms of this cutoff scale:

$$V_S(r;\mu_f) = -4\pi C_F \int_{q>\mu_f} \frac{d^3\vec{q}}{(2\pi)^3}\, e^{i\vec{q}\cdot\vec{r}} \frac{\alpha_V(q^2)}{q^2}\,. \tag{2.6}$$

Since all the known renormalons stem from the low energy region of the $\vec{q}$-integral, the above definition renders V_S free from renormalons.[2] In $V_S(r;\mu_f)$, there is a cutoff dependent part by construction, which is regarded as an IR sensitive part of V_S. Such a dependence vanishes only when it is combined with the IR quantities such as $\delta E_{\rm US}$. Hence, the mixing is induced through the factorization scale. In this respect the cutoff dependent part can be regarded as a renormalon related part. In contrast, the cutoff independent part is determined within perturbation theory independently of IR contributions, and hence it can be regarded as a genuine renormalon free part and as a pure UV contribution.

The renormalon free quantity, which we denote by $V_S^{\rm RF}(r)$ [= cutoff independent part of $V_S(r;\mu_f)$], can be constructed systematically as follows. For $\alpha_V(q^2)$ in eq. (2.6), we adopt the next-to-next-to-next-to-leading log ($\rm N^3LL$) result, which is obtained by RG improvement of the $\rm N^3LO$ fixed order result:

$$\alpha_V(q^2)|_{\rm N^3LL} = \alpha_s(q^2)\left[a_0 + a_1\frac{\alpha_s(q^2)}{4\pi} + a_2\left(\frac{\alpha_s(q^2)}{4\pi}\right)^2 + a_3^{\rm Reg.I\,or\,II}(q)\left(\frac{\alpha_s(q^2)}{4\pi}\right)^3\right], \tag{2.7}$$

where $\alpha_s(q^2)$ is the running coupling constant, namely, the solution to the RG equation at four-loop (for consistency):

$$q^2\frac{d}{dq^2}\alpha_s(q^2) = \beta(\alpha_s(q^2))|_{\text{4-loop}} = -\alpha_s(q^2)\sum_{i=0}^{3}\beta_i\left(\frac{\alpha_s(q^2)}{4\pi}\right)^{i+1}. \tag{2.8}$$

We solve this equation numerically.[3] The three-loop coefficient a_3 is originally IR divergent as mentioned and we regularize it with the prescription explained below [$a_3^{\rm Reg.I\,or\,II}(q)$ is given by eq. (2.19) or (2.20) in section 2.2]. Related to this divergence, the regularized a_3 has a q-dependence unlike the coefficients up to a_2. (As noted, this feature has nothing to do with renormalons.) We set $n_f = 3$ and the corresponding light quarks (u, d, s) are treated in the massless approximation in our main analysis. (Finite mass effects are taken into account as a systematic error of our α_s determination in section 3.3.) Up to here, the integrand of eq. (2.6) is determined. Then, by deforming the integration contour of eq. (2.6) in the complex q-plane, we can separate a cutoff independent part from a cutoff dependent part. We explain this formulation explicitly in appendix B, which is a brief review of refs. [15, 16]. After this procedure, we obtain the following expression:

$$V_S(r;\mu_f) = V_S^{\rm RF}(r) + \mathcal{C}_0(\mu_f) + \mathcal{C}_2(\mu_f)r^2 + \mathcal{O}(r^3)\,, \tag{2.9}$$

[2] More accurately, dominant renormalons which arise from the $\vec{q}$-integral are removed. Renormalons contained in $\alpha_V(q^2)$ are regarded as subdominant and have not been studied, to our knowledge. We neglect them in our analysis.

[3] Although the running coupling constant $\alpha_s(\mu^2)$ can approximately be expressed by series expansion in $1/\log(\mu^2/\Lambda^2_{\overline{\rm MS}})$, we do not use this approximation but solve the RG equation for $\alpha_s(\mu^2)$ numerically.

JHEP04(2019)155

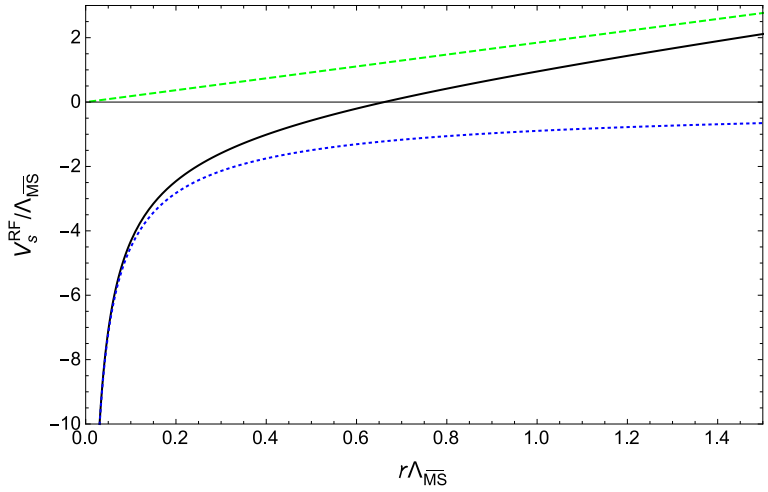

Figure 1. Renormalon free singlet potential $V_S^{\rm RF}/\Lambda_{\overline{\rm MS}}$ as a function of $\Lambda_{\overline{\rm MS}}r$ (black solid line). $V_C(r)/\Lambda_{\overline{\rm MS}}$ is shown by the blue dotted line, and the linear contribution $\mathcal{C}_1 r/\Lambda_{\overline{\rm MS}}$ [eq. (2.11)] is shown by the green dashed line. The results are obtained with regularization method I [eq. (2.19)].

where $V_S^{\rm RF}(r)$ is a μ_f-independent and renormalon-free quantity. The cutoff dependence of $V_S(r;\mu_f)$ is encoded in the r^0 and r^2 terms (and in further higher order terms), which correspond to the $u = 1/2$ and $u = 3/2$ renormalons, respectively. $V_S^{\rm RF}$ consists of a Coulomb-like part and a linear part:

$$V_S^{\rm RF}(r) = V_C(r) + \mathcal{C}_1 r\,. \tag{2.10}$$

$V_C(r)$ is expressed by a one-dimensional integral, whose explicit form is given in eq. (B.9). We evaluate this integral numerically. V_C has a Coulomb-like form with logarithmic corrections at short distances. The coefficient of the linear part, $\mathcal{C}_1$, is proportional to $\Lambda^2_{\overline{\rm MS}}$, and it can unambiguously be calculated as[4]

$$\mathcal{C}_1 = 1.844\Lambda^2_{\overline{\rm MS}} \quad \text{for} \quad n_f = 3 \quad \text{at N}^3\text{LL}\,. \tag{2.11}$$

One obtains $V_S^{\rm RF}/\Lambda_{\overline{\rm MS}}$ as a function of $\Lambda_{\overline{\rm MS}}r$ without free parameters, where $\Lambda_{\overline{\rm MS}}$ is the only dimensionful parameter in massless QCD. Here and hereafter, $\Lambda_{\overline{\rm MS}}$ is the Λ-parameter at four-loop in the $\overline{\rm MS}$ scheme with $n_f = 3$, unless otherwise stated: $\Lambda_{\overline{\rm MS}} = \Lambda_{\overline{\rm MS},n_f=3}^{\text{4-loop}}$. (See appendix C for the definition of $\Lambda_{\overline{\rm MS}}$.) We show $V_S^{\rm RF}(r)$ in figure 1.

So far, we have concentrated on the perturbative part V_S. Now let us see how the result is combined with the multipole expansion (2.1). Since we define the soft quantity V_S with the IR cutoff scale μ_f, it is natural to define the US quantity $\delta E_{\rm US}$ with the UV cutoff scale μ_f. Accordingly, the multipole expansion is written as

$$V_{\rm QCD}(r) = V_S(r;\mu_f) + \delta E_{\rm US}(r;\mu_f) + \dots\,. \tag{2.12}$$

It is confirmed in ref. [28] that the cutoff dependence of $V_S(r;\mu_f)$ of the r^2-term gets canceled against the leading cutoff dependence of $\delta E_{\rm US}(r;\mu_f)$ at the LL level. This corresponds

[4]The value is obtained in regularization I, where a_3 is regularized as in eq. (2.19).

JHEP04(2019)155

to the $u = 3/2$ renormalon cancellation, which was first reported in ref. [19]. Although the explicit confirmation at the N^{3}LL level (which we consider) is still missing, we assume a parallel scenario. Hence, by using eq. (2.9), we can perform the multipole expansion as

$$V_{\rm QCD}(r) = V_S^{\rm RF}(r) + \delta E_{\rm US}^{\rm RF}(r) + \dots \,. \tag{2.13}$$

Here, $\delta E_{\rm US}^{\rm RF}$ is the sum of $\delta E_{\rm US}(r;\mu_f)$ and $\mathcal{C}_2(\mu_f)r^2$; hence it is μ_f independent and free from renormalons. In this way, $V_S^{\rm RF}$ and $\delta E_{\rm US}^{\rm RF}$ are defined as genuine UV and IR quantities, respectively. We omit the constant $\mathcal{C}_0(\mu_f)$, which does not have a significant meaning in α_s determination; see section 3. Eq. (2.13) is the central formula of our theoretical calculation. The first term is given by eq. (2.10) and shown in figure 1. In our analyses, we regard $\delta E_{\rm US}^{\rm RF}$, which is an US quantity, as a nonperturbative object (non-local gluon condensate), and assume $\delta E_{\rm US}^{\rm RF} \sim \Lambda_{\overline{\rm MS}}^3 r^2$. This is because we focus on relatively long distances where $\Delta V \gg \Lambda_{\overline{\rm MS}}$ is in general *not* assured. The perturbative result for $\delta E_{\rm US}$ (obtained within pNRQCD) is used for a limited purpose. Hence, we treat the second term as $\delta E_{\rm US} = A_2 r^2$ where A_2 is a fitting parameter, showing the size of the (renormalon-free) nonperturbative effect.[5]

Let us state the unique features of $V_S^{\rm RF}$, which is a central object in eq. (2.13). First, let us clarify the difference from the usual RG improved predictions. Usual N^{k}LL predictions for the static QCD potential are reliable at short distances, but they have an unphysical singularity around $r \sim \Lambda_{\overline{\rm MS}}^{-1}$,[6] which distorts the behavior around this region drastically. In contrast, $V_S^{\rm RF}(r)$ does not have an unphysical singularity, while N^{3}LL accuracy is held at short distances. Therefore, reliable range of $V_S^{\rm RF}(r)$ on the low energy side is not limited a priori.[7] Secondly, $V_S^{\rm RF}$ does not have any renormalons. In particular, it is free not only from the $u = 1/2$ renormalon but also from the $u = 3/2$ renormalon, and thus, it is free from the leading r-dependent renormalon uncertainty of $\mathcal{O}(\Lambda_{\overline{\rm MS}}^3 r^2)$. Thanks to these features, $V_S^{\rm RF}$ is reliable at short to relatively long distances $\Lambda_{\overline{\rm MS}} r \sim \mathcal{O}(1)$. This allows our OPE prediction to have a wide validity range, as will be shown in section 3.2.2.

2.2 Treatment of US scale

We explain our prescriptions for regularizing the IR divergence in the three-loop coefficient. The IR divergence was first discovered in ref. [29] and calculated in ref. [30]. In dimensional regularization with $D = 4 - 2\epsilon$, it reads

$$\delta P_3 = 72\pi^2 \left(\frac{1}{\epsilon} + 6\log(\mu/q) \right) . \tag{2.14}$$

[5] The r^2 behavior may receive logarithmic corrections, for instance, from higher order computations of Wilson coefficients. We discuss their effects on α_s determination in appendix F.

[6] An N^{k}LL prediction is given by

$$r V_{\rm QCD}(r) = d_0 \alpha_s(1/r^2) + d_1 \alpha_s(1/r^2)^2 + \dots + d_k \alpha_s(1/r^2)^{k+1} \,,$$

where $\alpha_s(1/r^2)$ is the $(k+1)$-loop running coupling. Due to the singularity of $\alpha_s(1/r^2)$ around $r^{-1} \sim \Lambda_{\overline{\rm MS}}$, the prediction has an unphysical singularity.

[7] The naive expectation for the validity range of $V_S^{\rm RF}$ is the region up to where the $\Lambda_{\overline{\rm MS}}^3 r^2$ becomes non-negligible, due to the structure of the OPE.

JHEP04(2019)155

This IR divergence signals breakdown of naive perturbative expansion and is attributed to the dynamics at the US scale. The counterpart of the above divergence is provided from $\delta E_{\rm US}$ (2.5). Namely, the FT of $\delta E_{\rm US}(r)$ at $\mathcal{O}(\alpha_s^4)$, defined by

$$\delta E_{\rm US}(r)|_{\mathcal{O}(\alpha_s^4)} = -4\pi C_F \int \frac{d^3\vec{q}}{(2\pi)^3}\, e^{i\vec{q}\cdot\vec{r}} \frac{\widetilde{\delta E}_{\rm US}(q)|_{\mathcal{O}(\alpha_s^4)}}{q^2}\,, \tag{2.15}$$

is evaluated as [21]

$$\widetilde{\delta E}_{\rm US}(q)|_{\mathcal{O}(\alpha_s^4)} = \alpha_s \left(\frac{\alpha_s}{4\pi}\right)^3 \left(P_3^{\rm US} + \delta P_3^{\rm US}(\log(\mu/q))\right) \tag{2.16}$$

with

$$P_3^{\rm US} = 72\pi^2 \left(2\log(C_A\alpha_s(\mu)) + 2\gamma_E - \frac{5}{3}\right) \tag{2.17}$$

$$\delta P_3^{\rm US}(\log(\mu/q)) = -72\pi^2 \left(\frac{1}{\epsilon} + 6\log(\mu/q)\right)\,. \tag{2.18}$$

Namely, $\delta E_{\rm US}$ has the UV divergence $\delta P_3^{\rm US}$, and $\delta P_3^{\rm US} = -\delta P_3$. Hence, the sum of the soft contribution (V_S) and US contribution ($\delta E_{\rm US}$) at order α_s^4 is finite.

In our analysis, it is appropriate to remove the IR divergence (δP_3) from the definition of $V_S^{\rm RF}$ as well as its IR renormalons since $V_S^{\rm RF}$ is defined as a pure UV quantity. For this, we make the UV divergence of $\delta E_{\rm US}$ absorbed into V_S. This is compatible with our formulation since we define $\delta E_{\rm US}^{\rm RF}$ as a pure IR contribution.

We consider the following two prescriptions for regularizing the three-loop perturbative coefficient of V_S. In the first one, we regard $P_3^{\rm US} + \delta P_3^{\rm US}$, the perturbative contribution of $\delta E_{\rm US}$, as a UV contribution and make $V_S^{\rm RF}$ finite by including it as

$$\begin{aligned} a_3^{\rm Reg.I}(q) &\equiv (P_3 + \delta P_3) + (P_3^{\rm US} + \delta P_3^{\rm US})|_{\mu=q} \\ &= a_3 + 72\pi^2 \left(2\log(C_A\alpha_s(\mu^2)) + 2\gamma_E - \frac{5}{3}\right)\Big|_{\mu=q}\,. \end{aligned} \tag{2.19}$$

When RG improvement is applied, we also replace $\alpha_s(\mu^2)$ inside logarithm of eq. (2.19) by $\alpha_s(q^2)$, in the same way as in eq. (2.7). In the second prescription, we divide $P_3^{\rm US} + \delta P_3^{\rm US}$ into UV and IR contributions by a cutoff scale $\mu_{\rm US}$ which is taken above the US scale. In this case we adopt

$$a_3^{\rm Reg.II}(q) = a_3 + 144\pi^2 \log(\mu_{\rm US}/q)\,. \tag{2.20}$$

This can be compared to eq. (2.19) by regarding the regulator $C_A\alpha_s$ as $\Delta V(r)r \sim \mu_{\rm US}/q$. We choose $\mu_{\rm US} = 3\Lambda_{\overline{\rm MS}}$ or $4\Lambda_{\overline{\rm MS}}$.

The motivation to consider the above two prescriptions in α_s determination is to check sensitivity to the treatment of the US perturbative contribution. We will see that it does not induce a significant effect. We use the regularization I, given in eq. (2.19), in our main analysis.

JHEP04(2019)155

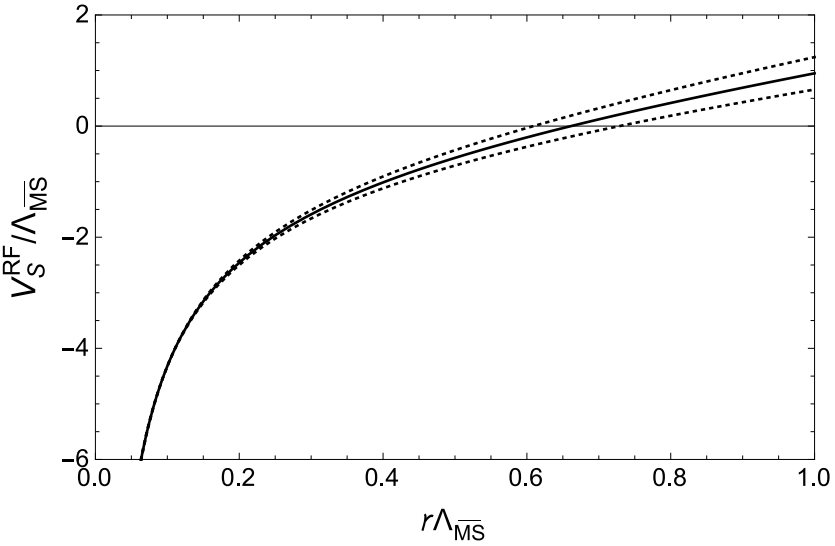

Figure 2. $V_S^{\rm RF}$ at N^{3}LL (solid) and the higher order uncertainty given by the region between the dotted lines. The r-independent constants are adjusted such that three lines take the same value at $\Lambda_{\overline{\rm MS}} r = 0.1$.

2.3 Higher order perturbative uncertainty

$V_S^{\rm RF}$, which we calculate at N^{3}LL accuracy, receives higher order corrections. We assume that $V_S^{\rm RF}$ can vary to

$$V_S^{\rm RF} \pm \delta V_S^{\rm RF}\,, \tag{2.21}$$

due to higher order corrections. We take $\delta V_S^{\rm RF}$ conservatively as

$$\delta V_S^{\rm RF} = V_S^{\rm RF}|_{\rm N^3LL} - V_S^{\rm RF}|_{\rm N^2LL}\,. \tag{2.22}$$

In calculating $V_S^{\rm RF}|_{\rm N^2LL}$, we use the 4-loop beta function[8] in evaluating $\alpha_V(q^2)$, while the fixed order results are used up to a_2 rather than up to a_3. Hence, $\delta V_S^{\rm RF}$ reduces to the Coulomb+linear part originating from the a_3-term alone (at N^{3}LL). We show the perturbative uncertainty of $V_S^{\rm RF}$ (i.e. $V_S^{\rm RF} \pm \delta V_S^{\rm RF}$) in figure 2.

Higher order uncertainty $\delta V_S^{\rm RF}$ takes a Coulomb+linear form (with log corrections) similarly to V_S. Hence, it is qualitatively different from the nonperturbative effect, whose form is quadratic in r. This enables us to estimate the nonperturbative effect while distinguishing it from the perturbative uncertainty.[9]

Furthermore, we note that the perturbative error is smaller than the one in usual perturbative calculation thanks to renormalon subtraction. We will revisit this point in section 3.2.2. We also remark that the higher order uncertainty is expected to become smaller as the order grows. Since such a property does not hold in the presence of renormalons, this is another non-trivial merit of renormalon subtraction.

[8] This is for simplicity of the analysis.

[9] In previous studies considering the OPE, an estimation of nonperturbative effect suffers significantly from perturbative uncertainty since renormalons are not subtracted from perturbative calculation. See section 3.2.2.

JHEP04(2019)155

3 α_s determination

We determine the strong coupling constant at the Z boson mass scale, $\alpha_s(M_Z^2)$. We achieve this by matching the theoretical calculation [presented in the previous section in particular in eq. (2.13)] with a lattice result. We perform two analyses.

The first analysis, which we call Analysis (I), consists of two steps. In the first step, we take the continuum limit of the lattice result (without referring to the theoretical prediction above). In the second step, we compare it with the theoretical prediction to extract $\alpha_s(M_Z^2)$. We proceed while checking (a) if the lattice result can smoothly be extrapolated to the continuum limit, and (b) if $V_S^{\rm RF}$ can explain the lattice result up to $\mathcal{O}(r^2)$ difference, consistently with the OPE structure of eq. (2.13). After confirming these features, we determine $\alpha_s(M_Z^2)$.

In the second analysis, Analysis (II), we perform a global fit to determine $\alpha_s(M_Z^2)$. The two tasks, i.e., an extrapolation to the continuum limit of the lattice data and a determination of α_s by comparison with the theoretical prediction, are carried out at once.

Our final result will be adopted from Analysis (II), where we achieve a smaller error than Analysis (I). Analysis (II) is a first-principle analysis, which avoids model interpolating function, required in Analysis (I) for continuum extrapolation. Nevertheless, Analysis (II) is performed without revealing detailed profiles at intermediate steps. To fill the gap, Analysis (I) is performed, where the intermediate steps of the analysis are examined and exhibited explicitly.

We start with an explanation of lattice simulations in section 3.1. Subsequently we present Analysis (I) in section 3.2 and Analysis (II) in section 3.3. Necessary formulas for the analyses are given in appendix D.

3.1 Lattice simulations

Our analysis is performed by using lattice QCD data $V_{\rm latt}(r)$ obtained by the JLQCD collaboration [24, 25]. Their numerical simulations are carried out in three-flavor QCD in the isospin limit by employing the Symanzik gauge [31] and Möbius domain-wall quark actions [32]. A careful choice of the detailed structure of the quark action reduces the computational cost to simulate fine lattices remarkably while preserving chiral symmetry to good precision [24]. Lattice data of $V_{\rm latt}$ are available at three lattice cutoffs, which are determined as $a^{-1} = 2.453(4)$, 3.610(9) and 4.496(9) GeV from the Wilson-flow scale [33]. In the following, we denote the three lattice spacings by a_1, a_2 and a_3 ($a_1 > a_2 > a_3$). Discretization errors of $V_{\rm latt}$ start at $O(a^2)$, since chiral symmetry forbids $O(a)$ errors.

The lattice sizes are $N_s^3 \times T = 32^3 \times 64$, $48^3 \times 96$ and $64^3 \times 128$ at a_1, a_2 and a_3, respectively. In order to control finite volume effects, their physical sizes are roughly kept constant $L = N_s a \approx 2.6\,\text{fm}$, and sufficiently larger than the short distance region $r \lesssim 0.5\,\text{fm}$, where we perform the matching with the OPE. At each cutoff, we take lattice data $V_{\rm latt}(r)$ at a single combination of the degenerate up and down quark mass m_{ud} and the strange quark mass m_s. While m_s is close to its physical value, m_{ud} corresponds to unphysically heavy pion mass $M_\pi \approx 300\,\text{MeV}$. The correction to $V_{\rm latt}(r)$ due to the unphysical quark masses is taken into account in Analysis (II), but turns out to be small (see section 3.3).

JHEP04(2019)155

a^{-1} [GeV]	size	m_{ud}	m_s	M_π [MeV]	M_K [MeV]	# bin
$a_1^{-1}=2.453(4)$	32×64	0.0070	0.0400	309(1)	547(1)	$N_1=200$
$a_2^{-1}=3.610(9)$	48×96	0.0042	0.0250	300(1)	547(2)	$N_2=100$
$a_3^{-1}=4.496(9)$	64×128	0.0030	0.0150	284(1)	486(1)	$N_3=100$

Table 1. Lattice simulation parameters. For the quark masses m_{ud} and m_s, we list bare values in lattice units. The renormalization factor to the $\overline{\text{MS}}$ scheme is available in ref. [34].

Gauge ensembles are generated by using the Hybrid Monte Carlo algorithm. The statistics are 5,000 Molecular Dynamics (MD) time at each simulation point. Simulation parameters are summarized in table 1.

The potential $V_{\text{latt}}(r)$ is extracted from the asymptotic behavior of the rectangular Wilson loop

$$W(r,t) = C(r)\,\exp\left[-V_{\text{latt}}(r)\,t\right] \quad (t\to\infty), \tag{3.1}$$

where r and t represent its spatial and temporal sizes, respectively. A gauge link smearing [35] is applied to the spatial Wilson lines to suppress excited state contaminations at reasonably small t. The spatial Wilson lines and, hence, the quark pair separation $\vec{r}$ are chosen to be parallel to the spatial directions $(1,0,0)$ and $(1,1,0)$, which we call direction $d=1$ and 2 in the following. Throughout this study, we estimate the statistical error by the jackknife method. The bin size is chosen as 25 (a_1) or 50 MD time (a_2 and a_3) by inspecting the bin size dependence of the jackknife error of V_{latt}. The number of bins is $N_1=200$ (a_1) or $N_2=N_3=100$ (a_2 and a_3). The statistical correlation is taken into account in the fit (3.1) and subsequent analyses.

3.2 Analysis (I): two-step analysis

In Analysis (I), we first take the continuum limit of the lattice data in section 3.2.1. Using the extracted result, we confirm the validity of the OPE and compare it with other methods adopted in preceding studies in section 3.2.2. Matching of the OPE with the lattice result to determine α_s is performed in section 3.2.3.

3.2.1 Continuum extrapolation

We take the continuum limit of the dimensionless combination $X_{\text{latt}}(r) \equiv r_1[V_{\text{latt}}(r) - V_{\text{latt}}(r_1)]$. Here, r_1 is the scale defined by $r_1^2\frac{dV}{dr}(r_1)=1$. We fix the r-independent constant by subtracting the value at $r=r_1$.[10]

To take the continuum limit $X_{\text{latt}}^{\text{cont}}(r) = X_{\text{latt}}(r;a=0)$, we first construct sequences $\{X_{\text{latt}}(r;a)\}_{a=a_1,a_2,a_3}$ with *physical distances* r fixed. We choose these reference distances r as the physical points where the coarsest lattice has original data.[11] To obtain $X_{\text{latt}}(r;a)$

[10] By subtracting the potential at $r=r_1$, we can eliminate the r-independent constant which exhibits a divergent behavior in the lattice simulations as $a\to0$.

[11] Namely, $X_{\text{latt}}(r;a)$ at reference distances is determined without extrapolating lattice data using model-assumption (3.2).

JHEP04(2019)155

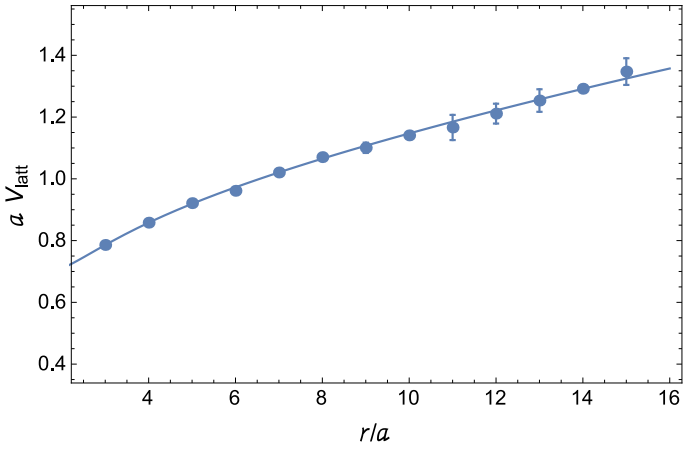

Figure 3. Interpolation of a jackknife lattice data for $d = 1$ and $i = 1$. The reduced χ^2 [defined in eq. (D.1)] is given by $\chi^2_{\rm Inter}|_{d=1,i=1}/\text{d.o.f.} = 6.9/(13-5)$.

for each a at a reference distance r, we interpolate the lattice data, which are originally discrete, and calculate $X_{\rm latt}(r;a)$ via the interpolating function. An extrapolation to the continuum limit of the sequence $\{X_{\rm latt}(r;a)\}_{a=a_1,a_2,a_3}$ can straightforwardly be performed once the sequence is constructed.

To interpolate the lattice data, we use the following function form:

$$V^{\rm Inter.}_{{\rm latt},d,i}(r) = \frac{\alpha_{d,i}}{r} + c_{0,d,i} + \sigma_{d,i}\, r + \frac{c_{1,d,i}}{r^3} + c_{2,d,i}\, r^2\,, \tag{3.2}$$

where $d = 1, 2$ and $i = 1, 2, 3$ specify the direction and lattice spacing, respectively. The first three terms represent the Cornell potential, which is consistent with the LO perturbation theory at short distances and consistent with the string model at long distances. If we assume this function form to be correct at the continuum limit, correction terms can arise due to finite a and L effects. The fourth term, $1/r^3$-term, is included to take into account the $\mathcal{O}(a^2)$ discretization error. (Note that the potential has mass dimension one.) The fifth term is similarly introduced for finite L effect to absorb a $1/L^3$-term. Furthermore, the lattice potential data are function of $\vec{r}$ rather than r, since the rotational symmetry is broken. Therefore, the coefficients can differ depending on the direction. We interpolate the lattice data separately for each direction. This is the reason why the subscript d appears in eq. (3.2).

In interpolation, we use the lattice data in the range $2a < r < L/2$. Namely, we do not use, for instance, the data at $r = a$. This aims at being free from serious finite a and L effects. (We show in appendix E that when we include the data at $r = a$, continuum extrapolation cannot be performed reasonably.) In fact, the function form (3.2) is chosen assuming the hierarchy $r/a \gg 1$ and $r/L \ll 1$.

From the fit, we obtain an interpolating function in a units. We show an example in figure 3, where one sees that the interpolating function can indeed fit the lattice data. We calculate $X_{\rm latt}(r;a)$ at reference distances using the interpolating function in lattice units: first, we calculate the ratio r_1/a from the (slope of) interpolating function, with which

JHEP04(2019)155

i (size)	$i=1$ ($32^3\times 64$)		$i=2$ ($48^3\times 96$)		$i=3$ ($64^3\times 128$)	
d ($N_{i,d}$)	$d=1$ (13)	$d=2$ (10)	$d=1$ (21)	$d=2$ (15)	$d=1$ (29)	$d=2$ (21)
χ^2/d.o.f	7.5/8	2.5/5	7.7/16	9.6/10	21.4/24	12.9/16
r_1/a	3.84(14)	3.93(16)	5.76(15)	5.59(12)	7.13(11)	7.121(98)
α	−0.59(77)	−0.31(64)	−0.74(23)	−0.60(20)	−0.45(11)	−0.577(91)
c_0 [GeV]	2.07(66)	1.87(56)	3.17(24)	2.96(23)	3.33(14)	3.50(12)
σ [GeV^2]	0.24(19)	0.28(17)	0.060(84)	0.169(81)	0.211(56)	0.139(50)
c_2 [GeV^3]	−0.004(18)	−0.008(16)	0.0223(85)	0.0065(91)	0.0036(68)	0.0136(60)
c_1 [GeV^{-2}]	0.11(33)	−0.03(25)	0.062(53)	0.043(42)	0.007(17)	0.029(13)

Table 2. Fitting parameters in eq. (3.2), r_1/a, and the reduced χ^2. The fitting parameters are shown as dimensionful quantities (except for α), which are originally obtained as dimensionless parameters normalized by proper powers of a. To make them dimensionful parameters, we use the lattice spacings estimated from the Wilson-flow scale. $N_{i,d}$ is the number of the lattice data used in interpolation.

one can convert the function into r_1 units. Secondly, we read off a value of $X_{\rm latt}(r)$ at a reference point.

By repeating the above procedure for all the jackknife samples, we obtain the average of $X_{\rm latt}(r;a)$ and its statistical error $\delta X_{\rm latt}(r;a_i)$ for each a at the reference distances r.[12] In our jackknife analysis, we ignore statistical fluctuation of the covariance matrix $[\Delta^{\rm latt}_{d,i}(r_k,r_j)]$, and use $[\Delta^{\rm latt}_{d,i}(r_k,r_j)]$ calculated with all the data for all the jackknife samples. Our analysis using the jackknife method proceeds in the same way hereafter.

In table 2, we summarize the fitting parameters in interpolation of eq. (3.2). Generally, we have smaller statistical errors for finer lattice since more data are available for the interpolation. The lattice spacings obtained via r_1/a are consistent with the ones determined from the Wilson-flow scale (where $r_1 = 0.311(2)$ fm is assumed [36–38]), although the former ones have much larger statistical errors.

Now we are in a position to extrapolate the sequences $\{X_{\rm latt}(r;a)\}_{a=a_1,a_2,a_3}$ to the continuum limit $a\to 0$. In figure 4, we plot the data point of $X_{\rm latt}(r;a)$ as a function of a^2/r_1^2, where we choose $r=3a_1$ and $r=8a_1$ from the analysis for $d=1$. We extrapolate the data by a linear fit in a^2, in accord with the $\mathcal{O}(a^2)$ discretization error. Namely, we extrapolate the lattice data at each reference distance to the continuum limit with

$$Y(a) = \gamma + \delta\cdot(a/r_1)^2\,, \tag{3.3}$$

where γ,δ are the fitting parameters. γ corresponds to $X^{\rm cont}_{\rm latt}$. In figure 4, one can see that the data follow this function and are extrapolated to the continuum limit. To see how smoothly the data are extrapolated to the continuum limit, we show the reduced χ^2 [i.e. $\chi^2_{\rm ex}$/d.o.f. of eq. (D.3)] at the reference distances in figure 5. Almost all the points

[12] More precisely, we choose the reference points as $r/r_1 = 3\langle a_1/r_1\rangle, 4\langle a_1/r_1\rangle, \ldots, 15\langle a_1/r_1\rangle$ for $d=1$, and similarly for $d=2$. Therefore, to calculate the average and statistical error of $X_{\rm latt}(r;a)$ at these distances, we first calculate $\langle a_1/r_1\rangle$ by examining all the jackknife samples of $i=1$. Then, we read off the values of $X_{\rm latt}(r;a)$ at these distances for each jackknife sample.

JHEP04(2019)155

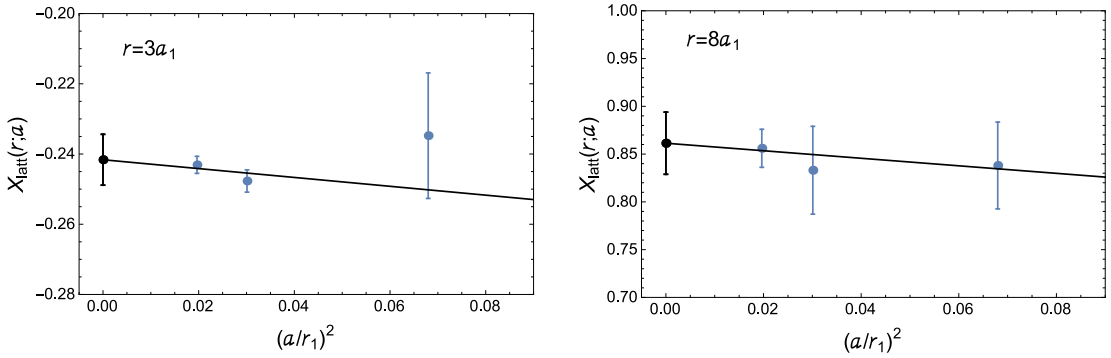

Figure 4. $X_{\rm latt}(r;a)$ as functions of $(a/r_1)^2$. We show them for $r = 3a_1$ (left) and $r = 8a_1$ (right), which appear in the analysis for $d = 1$, as examples. Black lines are linear functions in a^2, which extrapolate the data to the continuum limit. $\chi^2_{\rm ex}$/d.o.f., which is the reduced χ^2 in this extrapolation, are 1.43 (left) and 0.15 (right). The black data at $a = 0$ are the extracted continuum limit with the shown statistical errors.

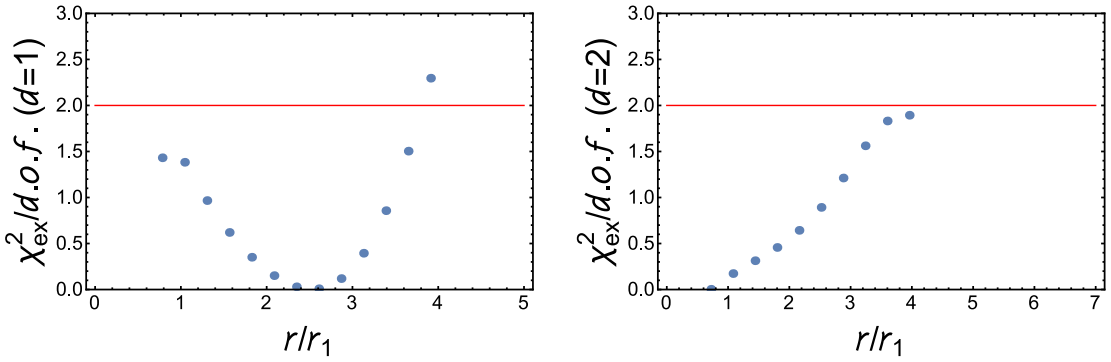

Figure 5. The reduced χ^2 in extrapolation [see eq. (D.3) for definition] for the distances where the continuum limit are taken. As a benchmark, χ^2/d.o.f. $= 2$ is shown by the red line.

are extrapolated to the continuum limit smoothly with the reduced χ^2 less than 2. Only the farthest data of $d = 1$, which has χ^2/d.o.f. > 2, is not adopted as our continuum limit result.

In this way, we obtain the continuum limit $X^{\rm cont}_{\rm latt}(r)$. It is shown in figure 6. We also list the numerical values in table 3. The covariance matrix for $X^{\rm cont}_{\rm latt}$ (as well as its definition) is presented in appendix D for the first 6 points in the short distance region.[13]

3.2.2 Consistency checks and comparison with conventional methods

Before determining α_s, we check consistency of the OPE as given in eq. (2.13) by using the lattice data $X^{\rm cont}_{\rm latt}$. First, we examine the perturbative part, $V_S^{\rm RF}$. We check whether $V_S^{\rm RF}$ has a reasonable behavior as we go to higher orders. For this purpose, we construct $V_S^{\rm RF}$ at LL to N^{2}LL in a parallel way to section 2.1[14] and compare them with the current order prediction at N^{3}LL. Note that, at N^{k}LL, the prediction $V_S^{\rm RF}/\Lambda^{(k+1)\text{-loop}}_{\overline{\rm MS}}$ is obtained as a

[13]The authors can provide a larger size matrix upon request.

[14]The perturbative potentials at N^{k}LL for $k = 0, 1, 2$ do not contain IR divergences.

JHEP04(2019)155

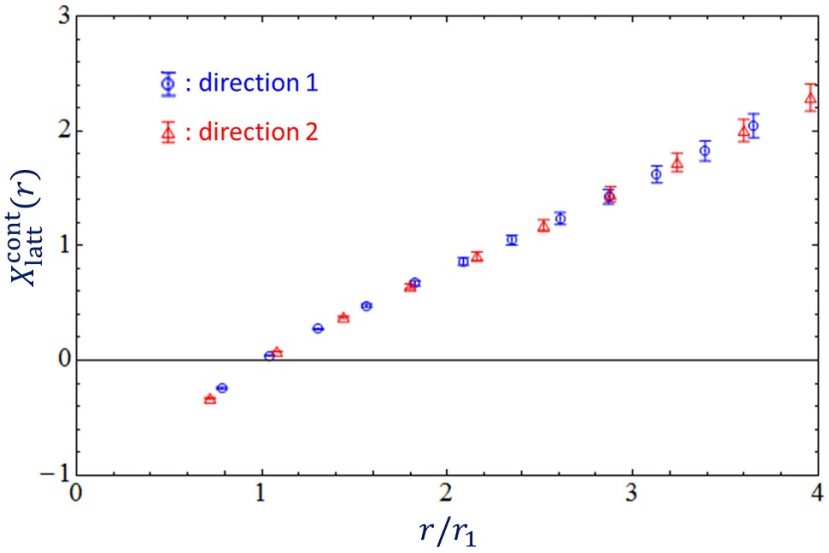

Figure 6. Continuum limit of the lattice result, $X^{\rm cont}_{\rm latt}$. Blue points originate from $d = 1$ and red ones from $d = 2$.

r/r_1	$X^{\rm cont}_{\rm latt}$
0.7196	−0.3305(93)
0.7822	−0.2416(72)
1.043	0.04211(15)
1.079	0.07662(33)
1.304	0.2723(48)
1.439	0.3775(83)
1.564	0.478(13)
1.799	0.645(22)
1.825	0.672(22)
2.086	0.861(33)
2.159	0.908(37)

r/r_1	$X^{\rm cont}_{\rm latt}$
2.347	1.049(43)
2.519	1.175(52)
2.607	1.236(52)
2.868	1.426(63)
2.878	1.448(66)
3.129	1.621(75)
3.238	1.725(81)
3.389	1.826(88)
3.598	2.004(97)
3.650	2.05(10)
3.958	2.29(12)

Table 3. Numerical results of $X^{\rm cont}_{\rm latt}(r)$.

function of $\Lambda^{(k+1)\text{-loop}}_{\overline{\rm MS}} r$. Therefore, in order to plot the k-th order prediction in $\Lambda^{4\text{-loop}}_{\overline{\rm MS}}$ units, we need a conversion parameter $\Lambda^{(k+1)\text{-loop}}_{\overline{\rm MS}}/\Lambda^{4\text{-loop}}_{\overline{\rm MS}}$. We determine these ratios by taking $\alpha_s(Q^2) = 0.2$ as an input regardless of the order of the running coupling (following ref. [15]), which yields $\Lambda^{1\text{-loop}}_{\overline{\rm MS}}/Q = 0.0305$, $\Lambda^{2\text{-loop}}_{\overline{\rm MS}}/Q = 0.0685$, $\Lambda^{3\text{-loop}}_{\overline{\rm MS}}/Q = 0.0648$, and $\Lambda^{4\text{-loop}}_{\overline{\rm MS}}/Q = 0.0642$. By regarding Q as a common scale, we obtain the ratios $\Lambda^{(k+1)\text{-loop}}_{\overline{\rm MS}}/\Lambda^{4\text{-loop}}_{\overline{\rm MS}}$ for $k = 0, 1, 2$. The above condition $\alpha_s(Q^2) = 0.2$ assures that different order predictions have no large deviations at $\Lambda^{4\text{-loop}}_{\overline{\rm MS}} r \sim 0.0642$. This is legitimate since these perturbative predictions should be accurate at such a high energy scale. In figure 7, we plot each order prediction in $\Lambda^{4\text{-loop}}_{\overline{\rm MS}}$ units, where the lattice result is shown as well. The lattice result $X^{\rm cont}_{\rm latt}$ is converted to $\Lambda_{\overline{\rm MS}}$ units from r_1 units by assuming $\Lambda_{\overline{\rm MS}} = \Lambda^{\rm PDG}_{\overline{\rm MS}} \equiv 336$ MeV

JHEP04(2019)155

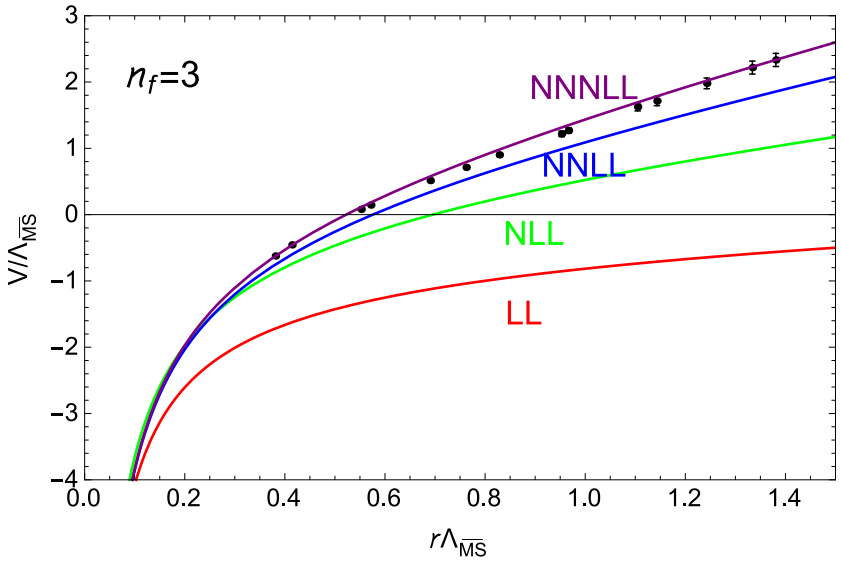

Figure 7. Comparison of the lattice result $X^{\rm cont}_{\rm latt}$ (black dots) with $V_S^{\rm RF}$ at LL (red), NLL (green), N^{2}LL (blue), and N^{3}LL (purple), for the inputs $n_f = 3$ and $\alpha_s(Q^2) = 0.2$. $\Lambda^{\rm PDG}_{\overline{\rm MS}} = 336$ MeV is used to convert $X^{\rm cont}_{\rm latt}$ to $\Lambda_{\overline{\rm MS}}$ units. r-independent constant of each potential is adjusted.

[which corresponds to the current PDG central value of $\alpha_s(M_Z^2)$], and using the central value of $r_1 = 0.311(2)$ fm. In plotting these theoretical predictions, the r-independent constants are adjusted such that the different order predictions have a common value at $\Lambda^{\text{4-loop}}_{\overline{\rm MS}} r = 0.0642$, and the N^{3}LL prediction matches the shortest distance lattice data. From the figure, one can see that the perturbative part, $V_S^{\rm RF}$, gradually approaches the lattice result at higher order.[15]

Now let us investigate a more detailed issue: we check if the difference between $V_S^{\rm RF}$ (at N^{3}LL) and the lattice result is $\mathcal{O}(r^2)$ as the OPE dictates. In figure 8, we show these two potentials in $\Lambda_{\overline{\rm MS}}$ units. The lattice potential is the same as the previous one. For the singlet potential, we add an r-independent constant so that the difference between them is zero at the origin. This constant is determined by a fit assuming that the difference follows const.+const.$\times r^2$.[16] We show their difference by the red boxes. In the difference, a linear-like behavior with an $\mathcal{O}(\Lambda^2_{\overline{\rm MS}})$ coefficient, which is observed in the lattice and perturbative potentials, vanishes. In fact, they can be fitted well by an r^2-term at short distances, as shown by the red line.[17] From this figure, the OPE turns out to be valid up to $\Lambda_{\overline{\rm MS}} r \lesssim 0.8$, corresponding to $r \lesssim 0.5$ fm or $r^{-1} \gtrsim 0.5$ GeV. We remark that this curve

[15] A similar behavior has been observed in quenched QCD in figure 17 of ref. [15] and figure 13 of ref. [39]. Compared to the quenched case, shorter distance lattice data are absent in the current three-flavor lattice simulation. Due to this, the coincidence of the lattice result and lower order predictions at short distances cannot be observed, which are observed in the quenched case.

[16] The first six points are used in this fit.

[17] The coefficient of the r^2-term (normalized by $\Lambda^3_{\overline{\rm MS}}$) is determined as

$$A_2/(\Lambda^{\rm PDG}_{\overline{\rm MS}})^3 = -0.222 \pm 0.011(\text{stat})\,. \tag{3.4}$$

The reduced χ^2 of this analysis is $\chi^2/\text{d.o.f.} = 2.5/(6-2)$.

JHEP04(2019)155

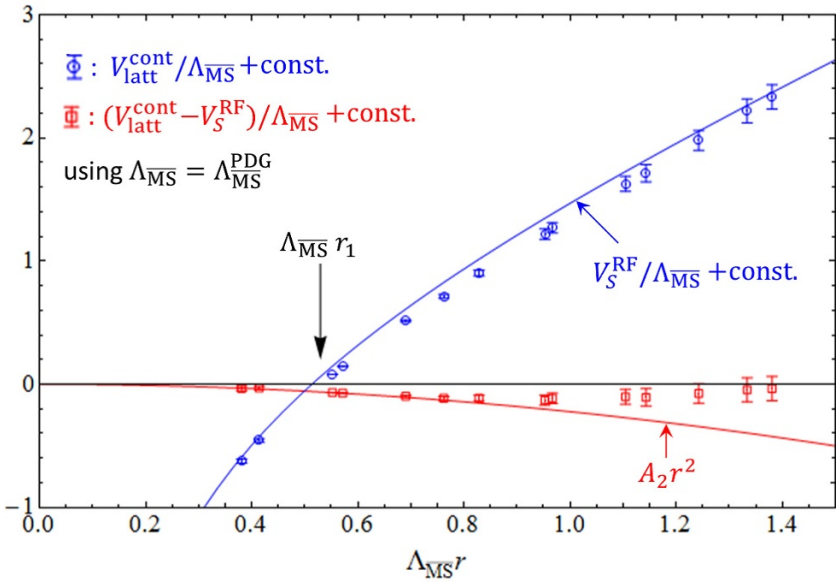

Figure 8. Comparison of the lattice result (cont. limit: blue circles) and leading OPE prediction ($V_S^{\rm RF}/\Lambda_{\overline{\rm MS}}$: blue line) using $\Lambda_{\overline{\rm MS}}^{\rm PDG}$ and adjusting r-independent part. The difference (red boxes) is fitted by const.$\times r^2$ (red line) at small r.

is almost unchanged even if we adopt the first 3 points in the fit, although we use the first 6 points in drawing the figure.

To clarify the impact of the above result, in figure 9 we compare the validity range of theoretical prediction with the methods adopted in the preceding analyses using the static potential. We first consider the case adopting the N^{3}LL prediction used in the main analysis of ref. [7], instead of $V_S^{\rm RF}$. The prediction in ref. [7] has the $u = 3/2$ renormalon and the unphysical singularity at $\Lambda_{\overline{\rm MS}} r \simeq 0.56$ unlike $V_S^{\rm RF}$, although it is free from the $u = 1/2$ renormalon.[18] Due to this singularity, the prediction cannot be obtained at $\Lambda_{\overline{\rm MS}} r \gtrsim 0.56$, and it starts to be distorted around this region as seen from the left panel of figure 9 (orange line). In the right panel, the difference from our continuum lattice result is shown (orange points). One cannot observe a const.+const.$\times r^2$ behavior even at $\Lambda_{\overline{\rm MS}} r \lesssim 0.6$.[19]

Secondly, we consider the fixed order perturbative prediction of V_S at N^{3}LO. It is free from the $u = 1/2$ renormalon (once a value at some distance is subtracted) and from the unphysical singularity, while it has the $u = 3/2$ renormalon. Since it is a fixed-order potential, the prediction is reliable only around the region $r \sim \mu^{-1}$. We choose μ as $\Lambda_{\overline{\rm MS}}/\mu = 0.4$, where μ^{-1} is close to the smallest r among the lattice data points in the continuum limit. This also fixes the value of $\alpha_s(\mu^2)$ as $\alpha_s(\mu^2) = 0.59$. In the right panel of

[18]The prediction of ref. [7] is obtained as follows. First, the fixed order perturbative prediction for the QCD force is considered, which is free from the $u = 1/2$ renormalon. Then, the RG improved potential is obtained by integrating the RG improved force with respect to r. Here, the RG improved force has a singularity due to the running coupling for the reason explained in footnote 6. Hence, the integration cannot be performed in the region containing this singularity.

[19]The determination of ref. [7] is performed at the high energy scale $\Lambda_{\overline{\rm MS}} r \lesssim 0.3$ after carefully examining the perturbative regime.

JHEP04(2019)155

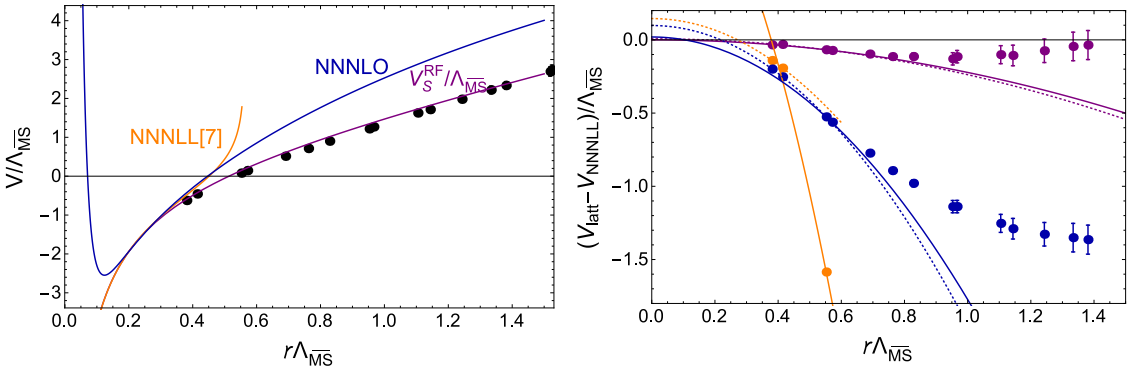

Figure 9. (Left) Static potentials obtained from lattice (black), $V_S^{\rm RF}/\Lambda_{\overline{\rm MS}}$ (purple), the N^{3}LL prediction of ref. [7] (orange), and the fixed order N^{3}LO prediction with $\Lambda_{\overline{\rm MS}}/\mu = 0.4$ (dark blue). (Right) Differences between the lattice result and the theoretical predictions. Purple data represent the difference from $V_S^{\rm RF}$, the orange ones from the N^{3}LL prediction of ref. [7], and the dark blue ones from the N^{3}LO prediction. The curves in this figure are const.+const.$\times r^2$ functions determined by fits. The purple solid line is determined with the first six points [χ^2/d.o.f. $= 2.5/(6-2)$], and the purple dotted one with the first three points [χ^2/d.o.f. $= 0.19/(3-2)$]. The orange solid line is determined with the first three points [χ^2/d.o.f. $= 85/(3-2)$], and the orange dotted one with the first two points [d.o.f. $= 0$]. The dark blue solid line is determined with the first six points [χ^2/d.o.f. $= 141/(6-2)$], and the dark blue dotted one with the first three points [χ^2/d.o.f. $= 0.002/(3-2)$].

figure 9, the difference from the lattice data is shown (dark blue points). We can observe the OPE structure up to a certain distance region: the first three points ($\Lambda_{\overline{\rm MS}} r \lesssim 0.55$) can be fitted reasonably by a const.+const.$\times r^2$ function, while the first six points ($\Lambda_{\overline{\rm MS}} r \lesssim 0.8$) cannot be. However, we note that the result of the analysis is sensitive to a choice of the renormalization scale. If we make the renormalization scale twice ($\Lambda_{\overline{\rm MS}}/\mu = 0.2$), the range that the OPE is applicable and the coefficient of an r^2-term vary considerably. (We cannot take the scale 1/2, since the running coupling constant diverges above this scale.) This indicates that the OPE structure is not held stable against the higher order correction. In contrast, if we perform a parallel analysis using $V_S^{\rm RF}$,[20] we always confirm that the OPE is valid up to $\Lambda_{\overline{\rm MS}} r \lesssim 0.8$ and the variation of the coefficient of an r^2-term is milder. Namely, the OPE structure is stably observed. This allows us to treat the nonperturbative effect (coefficient of an r^2-term) in a more reasonable and reliable way.

The above arguments show that our theoretical calculation indeed allows us to use a range up to larger r than previous studies. We confirmed that the OPE structure is observed up to $\Lambda_{\overline{\rm MS}} r \lesssim 0.8$. This is achieved thanks to a stable and reliable prediction of $V_S^{\rm RF}$ at short to relatively long distances. This feature originates from the RG improvement, the absence of the unphysical singularity, and the $u = 3/2$ renormalon subtraction. The latter two features result from subtraction of IR contributions [see eq. (2.6)] in constructing $V_S^{\rm RF}$. This subtraction removes instability caused by IR dynamics.

[20] Namely, we vary $\mu = q$ to $q/2$ or $2q$ in $\alpha_V(q^2)$ in obtaining the renormalon free part $V_S^{\rm RF}$.

JHEP04(2019)155

Discussion on r^2 behavior. We provide a supplementary explanation on at which level the OPE structure is confirmed in this study. The OPE of pNRQCD predicts that the difference between lattice result and $V_S^{\rm RF}$ is order r^2, and that a coefficient of a linear term in r is zero if it is considered. We investigate size of the coefficient, expected to be zero, by including a term $A_1 r$ in addition to $A_2 r^2$ for fitting the difference. We obtain $A_1/\Lambda^2_{\overline{\rm MS}} = -0.33 \pm 0.23({\rm stat})^{+0.25}_{-0.22}(\Lambda_{\overline{\rm MS}}) \pm 0.32({\rm h.o.}) = -0.33^{+0.47}_{-0.45}$, where the statistical and systematic errors are combined in quadrature. Here, we consider only the dominant systematic errors. The error associated with $\Lambda_{\overline{\rm MS}}$ is estimated by varying $\Lambda_{\overline{\rm MS}}$ within the current PDG error $\Lambda_{\overline{\rm MS}} = 336 \pm 17\,{\rm MeV}$; the other stems from higher order uncertainty of $V_S^{\rm RF}$, which is estimated by shifting $V_S^{\rm RF} \to V_S^{\rm RF} \pm \delta V_S^{\rm RF}$. One can see that A_1 is consistent with zero. In addition to this result, a fit with an r^2-term alone (assuming $A_1 = 0$) can be reasonably performed as shown above. These facts suggest correctness of the OPE.

At this stage, however, $A_1/\Lambda^2_{\overline{\rm MS}}$ of nearly order one is still allowed. Hence, we refrain from making a stronger statement on confirmation of the OPE structure before $A_1/\Lambda^2_{\overline{\rm MS}}$ is constrained to be much smaller than unity.[21]

Nevertheless, it is worth making a comment on an example of the hypothesis which conflicts with the OPE. One may find the literature where a nonperturbative linear potential with the coefficient of the string tension is considered *at short distances* $\Lambda_{\overline{\rm MS}} r \lesssim 0.8$. This possibility is excluded more than at 8 σ level from our estimate of A_1.[22]

3.2.3 α_s determination: matching between OPE and lattice result

We now determine $\alpha_s(M_Z^2)$ by matching the lattice result with the OPE. Our determination of α_s reduces to the problem to find an appropriate $x = \Lambda_{\overline{\rm MS}} r_1$ such that the OPE agrees with the lattice result. Once x is determined, we obtain $\Lambda_{\overline{\rm MS}}$ through the value $r_1 = 0.311(2)$ fm. Then, we obtain $\alpha_s(M_Z^2)$ by solving the RG equation for $\alpha_s(\mu^2)$.

We compare the lattice and theoretical potentials in $\Lambda_{\overline{\rm MS}}$ units by converting the lattice result to $\Lambda_{\overline{\rm MS}}$ units with x:

$$\tilde{X}^{\rm cont}_{\rm latt}(r) = x^{-1} X^{\rm cont}_{\rm latt}\,. \tag{3.5}$$

The OPE prediction is given by

$$v_{\rm OPE}(r) = \Lambda^{-1}_{\overline{\rm MS}} V_{\rm OPE}(r) = \Lambda^{-1}_{\overline{\rm MS}}[V_S(r) + A_0 + A_2 r^2]\,, \tag{3.6}$$

where A_0 and A_2 are the fitting parameters. In the matching, we choose the lattice data points satisfying $\Lambda^{\rm PDG}_{\overline{\rm MS}} r < 0.8$ in order for the OPE to be valid. Hence, the first six points of figure 6 are used. The covariance matrix required in this analysis is presented in appendix D.

The results are summarized in table 4. From the result of x in this table, we obtain

$$\Lambda_{\overline{\rm MS}} = 315 \pm 15({\rm stat})\ {\rm MeV}\,, \tag{3.7}$$

using $r_1 = 0.311\,{\rm fm}$.

[21] Our result for A_2, the coefficient of the r^2-term, is consistent with zero as well when systematic errors are considered. However, in fact, this value is dependent on a scheme to factorize a μ_f-independent part [16]. There always exists a scheme to render A_2 non-zero. Therefore, validity of the OPE, which predicts $\mathcal{O}(r^2)$ difference, is exclusively exhibited by smallness of A_1. (A_1 is independent of a scheme choice.)

[22] Here, we assume the string tension to be $\sigma_s/\Lambda^2_{\overline{\rm MS}} \sim 3.8$.

JHEP04(2019)155

x	0.496(24)
$A_0/\Lambda_{\overline{\rm MS}}$	0.580(44)
$A_2/\Lambda^3_{\overline{\rm MS}}$	0.04(22)
$\chi^2_{\rm match}$/d.o.f.	$0.4/(6-3)$

Table 4. Fitting parameters in Analysis (I). Values inside parentheses denote statistical errors. See eq. (D.5) for definition of $\chi^2_{\rm match}$.

The obtained 3-flavor $\Lambda_{\overline{\rm MS}}$ of eq. (3.7) gives the 5-flavor coupling as

$$\alpha_s(M_Z^2) = 0.1166^{+0.0010}_{-0.0011}(\text{stat})\,. \tag{3.8}$$

This value is obtained as follows. First, we calculate $\alpha_s(\mu^2)|_{n_f=3}$ below the charm $\overline{\rm MS}$ mass $\mu < \overline{m}_c = 1.3$ GeV, from the obtained $\Lambda_{\overline{\rm MS}}$ using eq. (C.1) in appendix C. Secondly, we obtain the 4-flavor coupling at the charm $\overline{\rm MS}$ mass (which we take as a matching scale) $\mu = \overline{m}_c$, using the 3-loop matching equation [40]. Then, we obtain $\alpha_s(\mu^2)$ for $\overline{m}_c < \mu < \overline{m}_b = 4.2$ GeV by solving the RG equation for $n_f = 4$. Similarly, we obtain the 5-flavor coupling at the bottom $\overline{\rm MS}$ mass by the matching equation. Then, we obtain the coupling at the Z boson mass $M_Z = 91.187$ GeV, $\alpha_s(M_Z^2)$, by solving the RG equation for $n_f = 5$. We solve the RG equation for $\alpha_s(\mu^2)$ numerically; see footnote 3.

For convenience, we summarize the conditions used in our main analysis, with which we determine the central value of $\alpha_s(M_Z^2)$.

- Controlling finite a and L effects: Lattice data in the range $2a < r < L/2$ are used in interpolation
- Interpolating function: Cornell type potential [eq. (3.2)]
- Lattice result extrapolated to $a = 0$: $X(r) = r_1[V_{\rm latt}(r) - V_{\rm latt}(r_1)]$
- Singlet potential: $V_S^{\rm RF}(r)$ defined by eq. (2.10), which has N^{3}LL accuracy
- Regularization of US divergence: Prescription I [eq. (2.19)]
- Matching range (Used lattice data in the continuum limit): $\Lambda^{\rm PDG}_{\overline{\rm MS}} r < 0.8$
- Conversion of x to $\Lambda_{\overline{\rm MS}}$: Central value of $r_1 = 0.311(2)$ fm

We now estimate systematic errors of our determination. For this purpose, we perform re-analyses by changing the conditions as follows and examine variations of determined $\alpha_s(M_Z^2)$.

- *Finite a effects.* We use the lattice data of $a < r < L/2$ in interpolation such that the shorter distance points $r \gtrsim a$ are included, although we still omit the data at $r = a$.[23]

[23] For the case including the data at $r = a$, see appendix E.

JHEP04(2019)155

- *Interpolating function.* The Cornell potential has a defect that it does not have a logarithmic correction in the Coulomb part at short distances where it should be $1/(r\log(r\Lambda_{\overline{\rm MS}}))$ rather than $1/r$. Such a logarithmic correction follows from the one-loop β function. We replace the Coulomb part by the one consistent with the one-loop β function:

$$V'^{\rm Inter.}_{\rm latt}(r) = V_C^{\text{large-}\beta_0}\left(r\Lambda_{\overline{\rm MS}}^{\text{1-loop}}\right) + c_0 + \sigma r + \frac{c_1}{r^3} + c_2 r^2\,, \tag{3.9}$$

  where $V_C^{\text{large-}\beta_0}(r)$ is the Coulomb-like potential calculated in the large-β_0 approximation according to the method of ref. [15] or appendix B. Its asymptotic form is given by[24]

$$\left[V_C^{\text{large-}\beta_0}/\Lambda_{\overline{\rm MS}}^{\text{1-loop}}\right](\rho = r\Lambda_{\overline{\rm MS}}^{\text{1-loop}}) \to \begin{cases} -C_F\frac{2\pi}{\beta_0}\frac{1}{\rho\log(1/\rho)} & (r\Lambda_{\overline{\rm MS}} \ll 1) \\ -C_F\frac{4\pi}{\beta_0\rho} & (r\Lambda_{\overline{\rm MS}} \gg 1)\,. \end{cases} \tag{3.11}$$

- *Subtraction point.* We take the continuum limit of

$$r_1[V_{\rm latt}(r) - V_{\rm latt}(0.8r_1)]\,, \tag{3.12}$$

  where the subtraction point is changed.

- *Higher order uncertainty.* We replace $V_S^{\rm RF}$ in matching as

$$V_S^{\rm RF} + t\delta V_S^{\rm RF} \tag{3.13}$$

  with $t = -1$ or 1 in order to estimate higher order uncertainty; see eq. (2.22) for $\delta V_S^{\rm RF}$.

- *US regularization.* We adopt the regularization prescription II, given by eq. (2.20). We choose $\mu_{\rm US}$ as $3\Lambda_{\overline{\rm MS}}$ and $4\Lambda_{\overline{\rm MS}}$.

- *Matching range.* We vary the range of the lattice result used in the matching as

$$\Lambda_{\overline{\rm MS}}^{\rm PDG} r < 0.7 \text{ or } 0.9 \tag{3.14}$$

  to examine the stability of the OPE truncated at $\mathcal{O}(r^2)$.

- r_1. We vary r_1 in the range $r_1 = 0.311 \pm 0.002$ fm.

The estimated systematic errors are summarized in table 5.

By taking the root-sum-square of the errors, we obtain

$$\alpha_s(M_Z^2) = 0.1166^{+0.0010}_{-0.0011}(\text{stat})^{+0.0018}_{-0.0017}(\text{sys}) \tag{3.15}$$

from Analysis (I).

[24] In interpolating the lattice unit potential with the above fitting form, we introduce $y = \Lambda_{\overline{\rm MS}}^{\text{1-loop}} a$ as the fitting parameter in order to convert $V_C^{\text{large-}\beta_0}/\Lambda_{\overline{\rm MS}}^{\text{1-loop}}$ to a units as

$$aV'^{\rm Inter.}_{\rm latt}(r) = y[V_C^{\text{large-}\beta_0}/\Lambda_{\overline{\rm MS}}^{\text{1-loop}}](yr/a) + \dots\,. \tag{3.10}$$

JHEP04(2019)155

	finite a	interpol. fn.	subt. point	h.o.	US	range	r_1
Obtained value	-4	$+4$	-8	$^{+14}_{-12}$ (t=−1) (t=1)	$^{+1}_{-0}$ ($3\Lambda_{\overline{\rm MS}}$) ($4\Lambda_{\overline{\rm MS}}$)	$^{+5}_{-8}$ (0.7) (0.9)	±1
Assigned error	±4	±4	±8	$^{+14}_{-12}$	±1	$^{+5}_{-8}$	±1

Table 5. Estimates of systematic errors in Analysis (I) from variations of the central value of $\alpha_s(M_Z^2)$ in units of 10^{-4} when varying the analysis conditions. In the upper row, variations are shown. (Detailed conditions are shown inside brackets). Assigned systematic errors are shown in the lower row.

3.3 Analysis (II): global fit

In Analysis (I), an interpolating function is assumed in order to take the continuum limit of the potential, although the exact functional form is unknown. This is a short-coming from the viewpoint of first principles. In Analysis (II), we perform a first-principle determination, without using such a model-like interpolating function. This is achieved by a global fit in which the continuum extrapolation and the matching with a theoretical calculation are performed at once.

This analysis is based on the idea that the OPE prediction should be correct at short distances and coincide with the lattice data once the discretization errors are removed. Then, the OPE is matched with the modified lattice data which can be regarded as the result in the continuum limit:

$$V_{\rm latt}^{\rm cont}(r) = V_{{\rm latt},d,i}(r) - \kappa_{d,i}\left(\frac{1}{r} - \left[\frac{1}{r}\right]_{d,i}\right) + f_d\frac{a_i^2}{r^3} - c_{0,d,i}\,. \tag{3.16}$$

Discretization errors contained in the original lattice data $V_{{\rm latt},d,i}$ are removed by the second and third terms (depending on i and d), and the last term adjusts the r-independent constant; $\left[\frac{1}{r}\right]$ is the LO result in the lattice perturbation theory, which deviates from a smooth $1/r$-function due to finite a and L effects. Hence, the second term removes the discretization error at the tree-level. Note that the tree-level potential is given by a one-gluon exchanging diagram and is order α_s. Here, κ is regarded as an effective coupling of lattice perturbation theory, and is treated as a fitting parameter. The third term extrapolates the data to the continuum limit by removing the remaining error of order $\alpha_s^2 a^2$. In eq. (3.16), we do not include a term related to finite L effects because in Analysis (I) the finite L effects, shown by the size of c_2, turn out to be small (see table 2). On the other hand, the term $f_d a_i^2/r^3$, which is also small in Analysis (I) (see c_1 in table 2), is kept just in case because Analysis (II) uses shorter distance data.

We perform matching by converting lattice and theoretical potentials to GeV units. Lattice data are converted to these units using a's estimated by the Wilson-flow scale. The theoretical potential is converted with $z = \Lambda_{\overline{\rm MS}}[{\rm GeV}]$, which is unknown in advance and thus is treated as a fitting parameter. Therefore, an OPE prediction used here is given by

$$V_{\rm OPE}(r) = z[V_S/\Lambda_{\overline{\rm MS}}](zr) + A_2 r^2\,. \tag{3.17}$$

Since an r-independent constant is already included in eq. (3.16), it is not included here.

JHEP04(2019)155

i (size)	$i=1$ ($32^3\times 64$)		$i=2$ ($48^3\times 96$)		$i=3$ ($64^3\times 128$)	
d ($N_{i,d}$)	$d=1$ (4)	$d=2$ (3)	$d=1$ (6)	$d=2$ (4)	$d=1$ (8)	$d=2$ (5)
κ	0.19(15)	−0.26(85)	0.27(12)	−0.53(88)	0.27(11)	−0.57(91)
c_0 [GeV]	2.245(11)	2.300(87)	3.012(11)	3.099(89)	3.546(10)	3.631(86)
χ^2	$\chi^2/\text{d.o.f.} = 8.7/(30-16)$ (global fit)					
f_d	$f_1 = 0.0004(18)$, $f_2 = -0.025(32)$ (common to all i)					
A_2	$A_2 = -0.0091(54)$ GeV^3 (common to all i,d)					

Table 6. Fitting parameters in Analysis (II). Only statistic errors are shown. $N_{i,d}$ expresses the number of data points for direction d of the i-th lattice.

In matching, we adopt the lattice data in the range $r\Lambda_{\overline{\text{MS}}}^{\text{PDG}} < 0.6$. Here, we choose a shorter distance region than in Analysis (I) since we have more available data points. It serves to reduce our dominant error, given by higher order perturbative uncertainty. In this analysis, we do not omit short distance data at $r \sim a$, and in particular we include the data at $r = a$. (Note that the continuum extrapolation cannot be taken reasonably if we include the data at $r = a$ in Analysis (I), as discussed in appendix E.) Thus, we take into account the tree-level correction, which is powerful to remove the discretization error at short distances (where perturbation theory works) and does not need the hierarchy $r \gg a$.[25] The number of the i-th lattice data used in the matching is $7, 10, 13$ points for $i = 1, 2, 3$, respectively.

In this analysis, we determine 16 parameters in total: $\Lambda_{\overline{\text{MS}}}$, A_2, six tree-level correction parameters κ's, two f's, and six r-independent constants c_0's. Due to the nature of this global fit, the lattice result in the continuum limit is determined such that it matches with the OPE prediction. In this respect, the continuum extrapolation is not taken within lattice simulation, but it is constrained by the OPE prediction.[26] Thus, the lattice data in the continuum limit in Analyses (I) and (II) have qualitatively different meanings.

In this global fit, we obtain

$$\Lambda_{\overline{\text{MS}}} = 334 \pm 10(\text{stat})\,\text{MeV}\,. \tag{3.18}$$

We summarize the other parameters in this global fit in table 6. The reduced χ^2 of this fit is $\chi^2_{\text{GF}}/\text{d.o.f.} = 8.7/(30-16)$ [see eq. (D.7) for definition of χ^2_{GF}], showing the validity of the analysis. A_2 is consistent with our previous estimate eq. (3.4), which is obtained while assuming $\Lambda_{\overline{\text{MS}}} = \Lambda_{\overline{\text{MS}}}^{\text{PDG}}$. (It is also consistent with Analysis (I).) f's are consistent with zero, which suggests that the discretization error is quite small after the tree-level correction is taken into account.

[25] In Analysis (I), the tree-level correction is not considered. It is because we try to examine the validity range of the OPE, and thus need the continuum limit result in a wide distance region, where the tree-level correction is not generally valid.

[26] We do not interpolate each lattice data (for each d and i). The continuous function appearing in this analysis is only the OPE prediction, and each lattice data is modified to agree with this function according to eq. (3.16).

JHEP04(2019)155

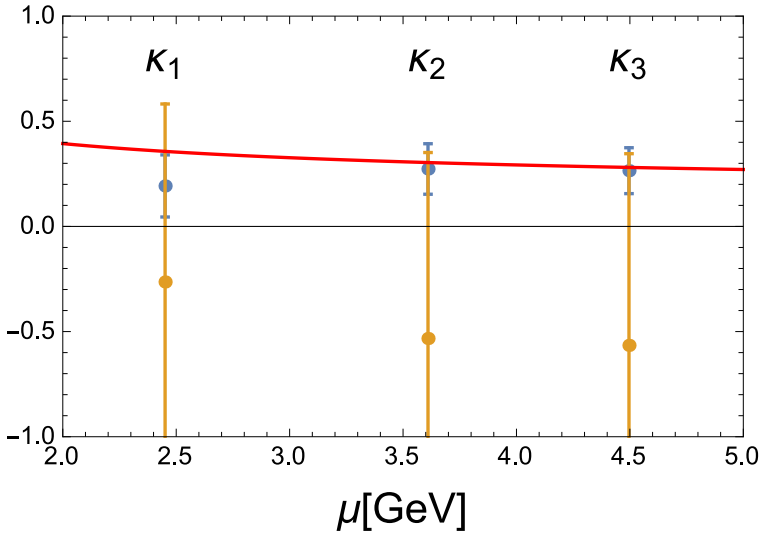

Figure 10. Determined values of κ. Blue (orange) data represent $\kappa_{i,d=1}$ ($\kappa_{i,d=2}$). Red curve represents the running of $C_F\alpha_s(\mu^2)$ assuming $\Lambda_{\overline{\rm MS}} = \Lambda^{\rm PDG}_{\overline{\rm MS}}$ and $n_f = 3$. We plot $\kappa_{d,i}$ at $\mu = a_i^{-1}$ for comparison.

To check if the tree-level correction works in a reasonable way, we show the determined values of κ's in figure 10. In this figure, we compare $\kappa_{d,i}$ with its naively expected value, $C_F\alpha_s(\mu^2)$, while taking the renormalization scale as $\mu = a_i^{-1}$. Note that $C_F = 4/3$ is multiplied since the LO result in the continuum theory is $V_{\rm QCD}(r)|_{\rm tree} = -C_F\alpha_s/r$. In plotting the running coupling, we assume $\Lambda_{\overline{\rm MS}} = \Lambda^{\rm PDG}_{\overline{\rm MS}}$ and $n_f = 3$. The determined κ's are consistent with the naively expected values within the statistical errors, which supports validity of our analysis. Large statistical errors for $\kappa_{d=2,i}$ stem from the small number of data for $d = 2$.

We show the lattice result in the continuum limit [eq. (3.16)] and the OPE prediction [eq. (3.17)] which are determined by the fit in figure 11. From the figure, one can see that the analysis is performed reasonably, and that the OPE calculation and the lattice result are mutually consistent in the examined region.

The obtained $\Lambda_{\overline{\rm MS}}$ in eq. (3.18) gives

$$\alpha_s(M_Z^2) = 0.1179 \pm 0.0007(\text{stat})\,. \tag{3.19}$$

The procedure to obtain $\alpha_s(M_Z^2)$ is the same as for Analysis (I).

For convenience, we summarize the conditions used in our main analysis, with which we determine the central value of $\alpha_s(M_Z^2)$.

- Controlling finite a effects: The data at $r \geq a$ are used combined with the tree-level correction.
- Singlet potential: $V_S^{\rm RF}(r)$ defined by eq. (2.10), which has N^{3}LL accuracy
- Regularization of US divergence: Prescription I [eq. (2.19)]

JHEP04(2019)155

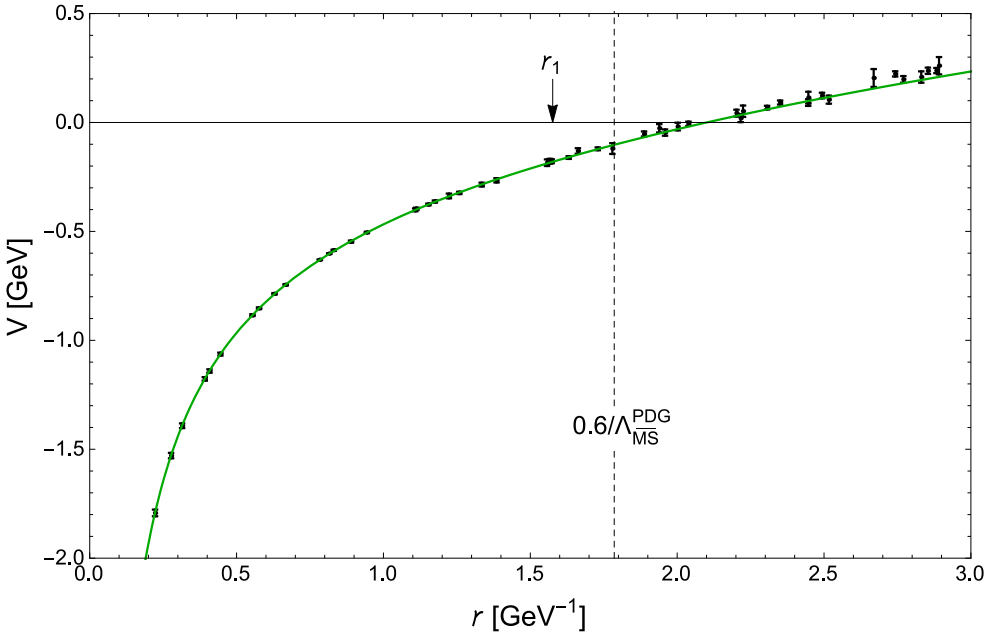

Figure 11. Lattice result in the continuum limit (black points) and the OPE calculation (green) determined simultaneously by the fit in Analysis (II). The distance region used in this fit $r\Lambda_{\overline{\rm MS}}^{\rm PDG} < 0.6$ is shown by the dotted line. For reference, $r = r_1$ is also shown.

- Quark masses: We use the lattice data obtained with unphysical quark mass inputs and $V_S^{\rm RF}$ in the massless quark approximation.
- Matching range: $\Lambda_{\overline{\rm MS}}^{\rm PDG} r < 0.6$

Now we estimate systematic errors of our determination. We perform the following reanalyses. Since this analysis will give our final result, some additional aspects are studied in comparison to Analysis (I).

- *Finite a effects.* We use the lattice data at $r \geq 2a$. In this case, we omit the tree-level correction by setting κ's to zero. This is because the role of the tree-level correction is similar to that of the a^2/r^3-term under the current hierarchy $a/r \leq 1/2$, where the tree-level correction is well approximated in expansion in a/r.[27]
- *Higher order uncertainty.* We replace $V_S^{\rm RF}$ in matching as

$$V_S^{\rm RF} + t\delta V_S^{\rm RF} \tag{3.20}$$

  with $t = -1$ or 1 in order to estimate higher order uncertainty; see eq. (2.22) for $\delta V_S^{\rm RF}$.
- *US regularization.* We adopt the regularization method II, given by eq. (2.20). We have chosen $\mu_{\rm US}$ as $3\Lambda_{\overline{\rm MS}}$ and $4\Lambda_{\overline{\rm MS}}$.

[27] If we include both κ's and f's, the fit is destabilized due to a flat direction caused by this degeneracy. We adopt the a^2/r^3-term rather than the tree-level correction since the tree-level correction becomes less reliable when the matching range shifts to lower energy region.

JHEP04(2019)155

- *Mass effects.* Lattice data are obtained with the unphysical mass inputs. We include an estimation of this mass difference effect as a systematic error, since we do not know the true correction. We estimate the lattice data on the physical point as

$$V_{\mathrm{latt},d,i}(r;m^{\mathrm{latt},i}) \to V_{\mathrm{latt},d,i}(r;\overline{m}) = V_{\mathrm{latt},d,i}(r;m^{\mathrm{latt},i}) + [V_{\mathrm{pt},i}(r;\overline{m}) - V_{\mathrm{pt},i}(r;m^{\mathrm{latt},i})]\,, \tag{3.21}$$

where $\overline{m}$ is the $\overline{\mathrm{MS}}$ masses for the light quarks (u,d,s); V_{pt} is the finite mass correction evaluated in perturbative QCD at N^{2}LO [41–43]. More precisely, it is a function of $\{r,m,\mu\}$ of the form

$$V_{\mathrm{pt}}(r;m) = c_1(r,m)\alpha_s^2 + c_2(r,m,\mu)\alpha_s^3\,, \tag{3.22}$$

which vanishes in the limit $m \to 0$. In the above estimation, we take the renormalization scale as $\mu = a_i^{-1}$ and choose α_s as 0.27, 0.23, 0.21 for $i = 1,2,3$, respectively, so that it is close to $\alpha_s(\mu^2 = a_i^{-2})$. For the $\overline{\mathrm{MS}}$ mass values of the light quarks, we use $\overline{m}_u = 2.2$ MeV, $\overline{m}_d = 4.7$ MeV, $\overline{m}_s = 96$ MeV. To model a nonperturbative effect, we also substitute a constituent quark mass of 300 MeV for $\overline{m}$ in eq. (3.21) as an additional test (while the other parameters are kept fixed). Furthermore, since V_S^{RF} is obtained by treating the light quarks as massless, the finite mass effects are also added to V_S^{RF} as

$$V_S^{\mathrm{RF}} \to V_S^{\mathrm{RF}} + V_{\mathrm{pt}}(r;\overline{m})\,. \tag{3.23}$$

For this V_{pt}, we take $\mu = 3$ GeV and $\alpha_s = 0.25$. In this way, we estimate both theoretical prediction and lattice result at the physical point.

- *Matching range.* We vary the range of the lattice result used in the matching as

$$\Lambda_{\overline{\mathrm{MS}}}^{\mathrm{PDG}} r < 0.5 \text{ or } 0.8 \tag{3.24}$$

to examine the stability of the OPE truncated at $\mathcal{O}(r^2)$.

- *Factorization scheme.* In extracting the renormalon free part V_S^{RF}, we rewrite the integrand of V_S by a complex function; see (B.2) in appendix B. In general, there can be other choices for this function, and in this regard, we have chosen a certain scheme. A different scheme practically causes an $\mathcal{O}(r^3)$ difference in the OPE prediction truncated at $\mathcal{O}(r^2)$; see ref. [16] for details.[28] To see an effect of this scheme dependence, we add an $A_3 r^3$-term in the fit so that this scheme dependence is absorbed. (Note that, in order to determine coefficients up to higher orders in r, a wider fitting range is required. We choose the range in this analysis as $\Lambda_{\overline{\mathrm{MS}}}^{\mathrm{PDG}} r < 0.8$, where A_2 and A_3 are stable against variation of the range.[29])

- *Lattice spacing.* The lattice spacing a, used to convert r and V_{latt} into physical units, has an error as shown in table 1, and has an additional error of 1.7% due to the uncertainty of the physical value of the Wilson-flow scale [44]. For the former

[28] In ref. [16], it is shown that the current choice is natural from the viewpoint of analyticity.
[29] This range is chosen after studying the stability for various ranges.

JHEP04(2019)155

	finite a	h.o.	US	Mass	range	fact. scheme	latt. spacing
Obtained value	-2	$^{+12}_{-10}$ $(t{=}-1)$ $(t{=}1)$	$^{+2}_{+0}$ $(3\Lambda_{\overline{\rm MS}})$ $(4\Lambda_{\overline{\rm MS}})$	$-0(^{\overline{\rm MS}\text{mass}}_{\text{Constituent mass}})$	$^{-3}_{-4}$ (0.5) (0.8)	$+3$	±4
Assigned error	±2	$^{+12}_{-10}$	±2	±0	±4	±3	±4

Table 7. Estimates of systematic errors in Analysis (II) from variations of the central value of $\alpha_s(M_Z^2)$ in units of 10^{-4} when varying the analysis conditions. In the upper row, variations are shown. (Detailed conditions are shown inside brackets). Mass effects are negligibly small in both cases. Assigned systematic errors are shown in the lower row.

one, the error is etimated by the largest deviation detected from a set of six data, $\{\{a_1 \pm \delta a_1, a_2, a_3\}, \{a_1, a_2 \pm \delta a_2, a_3\}, \{a_1, a_2, a_3 \pm \delta a_3\}\}$, where δa_i denotes the error shown in table 1. The error associated with the latter is estimated by shifting all the a's simultaneously by its uncertainty. By combining these two errors in $\alpha_s(M_Z^2)$ in quadrature, the uncertainty from the lattice spacing is estimated.

The estimated systematic errors are summarized in table 7. Some error sources included in Analysis (I) are absent thanks to the first-principle nature of this analysis. In addition, most of the systematic errors are reduced compared to Analysis (I). In particular, the higher order uncertainty is smaller since a shorter distance region is used; see figure 2. The mass effects turn out to be negligibly small even if we consider the constituent quark mass. This is because we are probing a sufficiently short-distance region. (Additional analyses on systematic errors are given in appendix F.)

As a result of Analysis (II), we obtain

$$\alpha_s(M_Z^2) = 0.1179 \pm 0.0007(\text{stat})^{+0.0014}_{-0.0012}(\text{sys})\,. \tag{3.25}$$

3.4 Summary of results

We have performed two determinations of α_s. In Analysis (I), which is a preparatory analysis, we first took the continuum limit of the lattice data, and then we matched the result with the OPE prediction. Although this analysis partially relies on a model-like assumption, we explicitly showed that (a) the continuum extrapolation of the lattice data can be taken smoothly, and that (b) the OPE combined with our renormalon subtraction is indeed consistent; see figure 8. We obtained $\Lambda_{\overline{\rm MS}} = 315 \pm 15(\text{stat})^{+26}_{-25}(\text{sys}) = 315^{+30}_{-29}\,\text{MeV}$ and $\alpha_s(M_Z^2) = 0.1166^{+0.0010}_{-0.0011}(\text{stat})^{+0.0018}_{-0.0017}(\text{sys}) = 0.1166^{+0.0021}_{-0.0020}$. The total errors are obtained by combining the statistic and systematic errors in quadrature.

In Analysis (II), we performed a global fit, where theoretical constraints are fully used. Analysis (II) is superior to Analysis (I) in the sense that it is a first-principle analysis and that our dominant error, higher order uncertainty, is reduced thanks to the use of short distance range. This gives our final result:

$$\begin{cases} \Lambda_{\overline{\rm MS}} = 334 \pm 10(\text{stat})^{+21}_{-18}(\text{sys})\,\text{MeV} = 334^{+23}_{-21}\,\text{MeV}\,, \\ \alpha_s(M_Z^2) = 0.1179 \pm 0.0007(\text{stat})^{+0.0014}_{-0.0012}(\text{sys}) = 0.1179^{+0.0015}_{-0.0014}\,. \end{cases} \tag{3.26}$$

One can see that both analyses give consistent values. Our results of $\alpha_s(M_Z^2)$ are compared with the current PDG and FLAG results in figure 12, where one can see that our results are also consistent with them.

JHEP04(2019)155

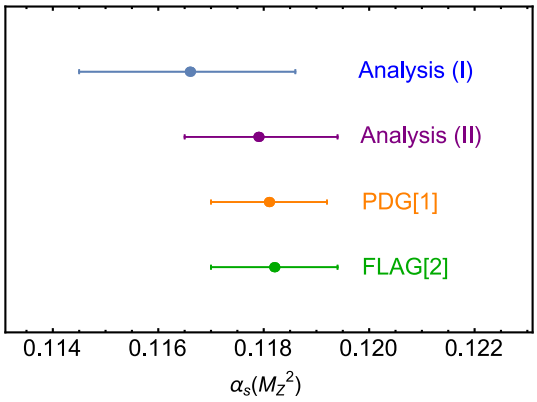

Figure 12. Comparison of various α_s determinations.

4 Conclusions and discussion

We determined the strong coupling constant α_s from the static QCD potential by matching a lattice result with a new OPE calculation where renormalons are subtracted from the leading Wilson coefficient. We subtract both $u = 1/2$ and $u = 3/2$ renormalons from the Wilson coefficient. In particular, we confirmed the following features regarding the renormalon subtraction.

1. Theoretically the cancellation of the $u = 3/2$ renormalon against the nonperturbative term is checked at the LL order. Furthermore, logarithmic contributions at IR region in the Fourier integral, which cause factorial divergence, are subtracted at the NNNLL level.

2. To check that ignoring renormalons contained in $\alpha_V(q)$ is harmless at the current level of the analysis, we confirmed that the renormalon-free Wilson coefficient $V_S^{\rm RF}(r)$ approaches the lattice data as we raise the order: LL, NLL, NNLL, NNNLL (figure 7).

3. As a result of the renormalon subtraction, convergence and stability against scale variation are improved as compared to the conventional methods. The difference between the Wilson coefficient $V_S^{\rm RF}(r)$ and the lattice data can be fitted with r^2 consistently with the prediction of the OPE. This r^2 behavior is observed up to $\Lambda_{\overline{\rm MS}} r \sim 0.8$ ($r \sim 0.4$ fm). (Figures 8, 9)

Based on these confirmations, we adopt the OPE framework where a power correction term of order r^2 is added to the renormalon-free Wilson coefficient.

In our α_s determination, the matching range is taken as $\Lambda_{\overline{\rm MS}} r \lesssim 0.6$ based on the above observation. This range is significantly wider than preceding determinations using the static QCD potential, where typically $\Lambda_{\overline{\rm MS}} r \lesssim 0.3$ has been used. This enables us to use the data not only at $r \sim a$ but also at $r \gg a$, where lattice simulation is considered to be accurate. We performed a reasonable fit in this wide region, which leads to a reliable determination. Our final result is $\alpha_s(M_Z^2) = 0.1179^{+0.0015}_{-0.0014}$. This result is obtained by a global fit [Analysis (II)] and is consistent with our another analysis [Analysis (I)], where

JHEP04(2019)155

we examined intermediate processes step by step. The reasonable value of α_s with respect to today's other determinations again indicates the validity of our analysis. We also confirmed that although the energy region extends to lower energy side than conventional determinations using perturbative calculation, varying the matching range does not induce significant systematic errors.

Dominant error of our determination comes from systematic errors, in particular from the higher order perturbative uncertainty of the leading Wilson coefficient. We emphasize that a finer lattice simulation will straightforwardly reduce this error, since we can adopt a shorter distance range in the fit, where the uncertainty becomes smaller.[30,31]

We believe that our analyses are useful not only in determining α_s but also in promoting understanding on the OPE structure and lattice discretization errors. As stated, this is a first numerical observation that the difference between the Wilson coefficient and the lattice result is consistent with $\mathcal{O}(r^2)$ behavior at $\Lambda_{\overline{\rm MS}} r \lesssim 0.8$ in accordance with the OPE structure. We also give a constraint on the linear term in r in the difference, which should be zero in the OPE. (See discussion in section 3.2.2.) Concerning the lattice discretization error, we clarified that (i) the data at $r = a$ indeed has a serious finite a effect (appendix E), and (ii) once the tree-level correction is considered combined with the OPE calculation, the finite a effect can be largely removed with reasonable values of lattice effective couplings.

Acknowledgments

The authors are grateful to the JLQCD collaboration for providing the lattice data. They thank G. Mishima for collaboration at an early stage of this study and also thank S. Aoki, S. Hashimoto, T. Onogi, and S. Sasaki for fruitful discussion. The works of Y.K. and Y.S. are supported in part by Grant-in-Aid for scientific research (Nos. 26400255 and 17K05404) from MEXT, Japan.

A Coefficients of perturbative calculation

The coefficients a_n of eq. (2.4) are given by

$$
\begin{aligned}
a_0 &= 1\,, \\
a_1 &= \frac{31}{3} - \frac{10}{9} n_f\,, \\
a_2 &= \frac{4343}{18} + 36\pi^2 + 66\zeta_3 - \frac{9\pi^4}{4} - \left(\frac{1229}{27} + \frac{52}{3}\zeta_3\right) n_f + \frac{100}{81} n_f^2\,, \\
a_3 &= a_3^{(0)} + a_3^{(1)} n_f + a_3^{(2)} n_f^2 + a_3^{(3)} n_f^3\,,
\end{aligned}
\tag{A.1}
$$

[30] Reduction of the higher order uncertainty can be estimated as follows. The relative perturbative accuracy in our formulation at N^{3}LL is order $\alpha_s(\mu^2)^4$, not affected by renormalon uncertainties. Here, μ is the typical scale used in the α_s determination. For instance, suppose that currently $\mu \sim 7\Lambda_{\overline{\rm MS}}$, and suppose that μ can be raised by a factor 2 (corresponding to twice finer lattices). Then the perturbative error would reduce, which is multiplied by $[\alpha_s((2\mu)^2)/\alpha_s(\mu^2)]^4 \sim 0.3$–$0.4$.

[31] We remark that if the coarsest lattice becomes finer while the finest lattice spacing is kept fixed, it serves to reduce the error. This is because our current range $\Lambda_{\overline{\rm MS}} r < 0.6$ is chosen so that the number of data points from the coarsest lattice is sufficient.

JHEP04(2019)155

with

$$
\begin{aligned}
a_3^{(0)} &= \frac{385645}{108} + \pi^2\left[\frac{893}{3} + 816\alpha_4 + (1844 - 1302\zeta_3)\log 2 + 295\zeta_3\right] + 5256\zeta_3 \\
&\quad + \pi^4\left(-\frac{227}{20} + 115\log 2 + 35\log^2 2\right) - \frac{17343}{2}\zeta_5 - \frac{1643\pi^6}{168} - \frac{3861\zeta_3^2}{2} + 3888 s_6\,, \\
a_3^{(1)} &= -\frac{452213}{324} + \pi^2\left[\frac{274}{27} - \frac{409}{9}\zeta_3 - 144\alpha_4 + \left(-\frac{8}{3} - 28\zeta_3\right)\log 2\right] - \frac{26630\zeta_3}{27} \\
&\quad + \pi^4\left(-\frac{293}{18} - \frac{35}{18}\log 2 + \frac{17}{6}\log^2 2\right) + \frac{30097}{36}\zeta_5 + \frac{1931}{1260}\pi^6 + \frac{513}{4}\zeta_3^2 - 216 s_6\,, \\
a_3^{(2)} &= \frac{93631}{972} + \frac{16\pi^4}{45} + \frac{412\zeta_3}{9}\,, \\
a_3^{(3)} &= -\left(\frac{10}{9}\right)^3\,.
\end{aligned}
\tag{A.2}
$$

Here, α_4 and s_6 are given by

$$
\alpha_4 = \mathrm{Li}_4(1/2) + \frac{(-\log 2)^4}{4!} = 0.527097\ldots\,, \tag{A.3}
$$

$$
s_6 = \zeta(-5,-1) + \zeta(6) = 0.987441\ldots\,. \tag{A.4}
$$

The above analytic expression for a_3 has been obtained in ref. [23].

B Formulation to extract $V_S^{\mathrm{RF}}(r)$ from $V_S(r)$

We explain the formula to extract $V_S^{\mathrm{RF}}(r)$ from eq. (2.6). We reduce eq. (2.6) to the one-dimensional integral representation:

$$
V_S(r;\mu_f) = -\frac{2C_F}{\pi r}\int_{\mu_f}^{\infty}\frac{dq}{q}\sin(qr)\alpha_V(q^2)\,, \tag{B.1}
$$

with $q = |\vec{q}|$. We rewrite the integral as

$$
\begin{aligned}
V_S(r;\mu_f) &= -\frac{2C_F}{\pi r}\mathrm{Im}\int_{\mu_f}^{\infty}\frac{dq}{q}e^{iqr}\alpha_V(q^2) \\
&= -\frac{2C_F}{\pi r}\mathrm{Im}\left(\int_{C_a} - \int_{C_b}\right)\frac{dq}{q}e^{iqr}\alpha_V(q^2)\,.
\end{aligned}
\tag{B.2}
$$

The contours C_a and C_b are displayed in figure 13. The integral along C_a is clearly independent of μ_f. Although the integral along C_b looks μ_f dependent, it contains a μ_f-independent part. We evaluate this integral as

$$
\frac{2C_F}{\pi r}\mathrm{Im}\int_{C_b}\frac{dq}{q}e^{iqr}\alpha_V(q^2) = \frac{2C_F}{\pi r}\mathrm{Im}\int_{C_b}\frac{dq}{q}\left[1 + iqr - \frac{1}{2}(qr)^2 - \frac{i}{6}(qr)^3 + \ldots\right]\alpha_V(q^2)\,, \tag{B.3}
$$

since $|qr| < \mu_f r \ll 1$. In expansion of the exponential factor, the real and pure imaginary coefficients appear in turn.

JHEP04(2019)155

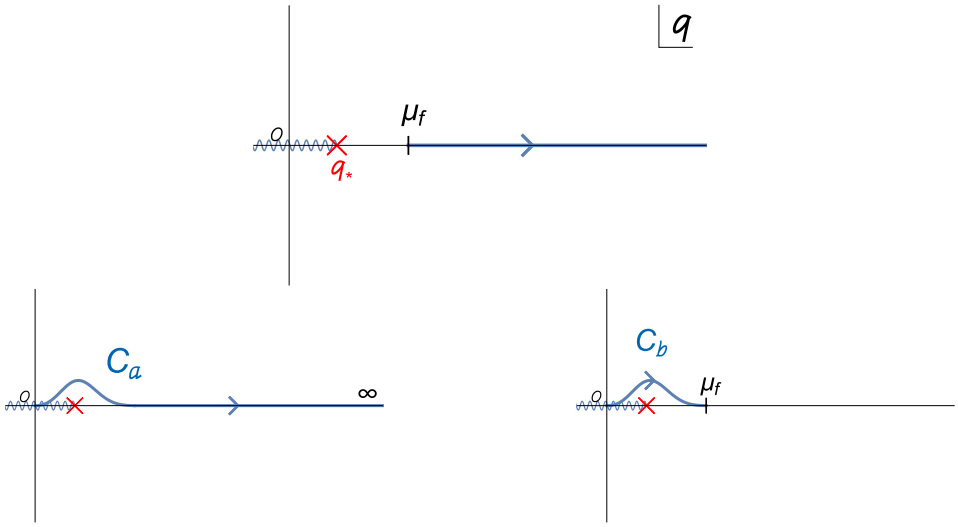

Figure 13. Contour C_a and C_b in the complex q-plane. q_* shows the singular point of $\alpha_V(q^2)$.

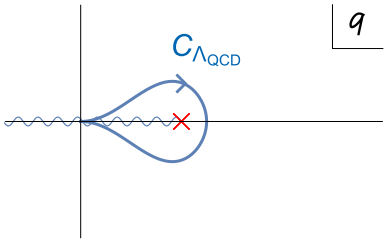

Figure 14. Contour $C_{\Lambda_{\rm QCD}}$.

The terms with real coefficients satisfy the relation $\{f(z)\}^* = f(z^*)$. Owing to this, these parts can be calculated as

$$\frac{2C_F}{\pi r}\mathrm{Im}\int_{C_b}\frac{dq}{q}\left[1-\frac{1}{2}(qr)^2\right]\alpha_V(q^2) = \frac{2C_F}{\pi r}\frac{1}{2i}\int_{C_{\Lambda_{\rm QCD}}}\frac{dq}{q}\left[1-\frac{1}{2}(qr)^2\right]\alpha_V(q^2)$$
$$= \frac{1}{r}\mathcal{C}_{-1} + \mathcal{C}_1 r \tag{B.4}$$

with

$$\mathcal{C}_{-1} = 2C_F\frac{1}{2\pi i}\int_{C_{\Lambda_{\rm QCD}}}\frac{dq}{q}\alpha_V(q^2)\,, \tag{B.5}$$

$$\mathcal{C}_1 = -C_F\frac{1}{2\pi i}\int_{C_{\Lambda_{\rm QCD}}}\frac{dq}{q}q^2\alpha_V(q^2)\,, \tag{B.6}$$

where $C_{\Lambda_{\rm QCD}}$ is shown in figure 14. The coefficients $\mathcal{C}_{-1}$ and $\mathcal{C}_1$ are μ_f independent and real. Numerical evaluation of these coefficients is sufficient for our purpose. [$\mathcal{C}_1$ is given by eq. (2.11).] We remark that the analytical results up to N^{2}LL can be found in ref. [15].

JHEP04(2019)155

On the other hand, the terms with imaginary coefficients do *not* satisfy the relation $\{f(z)\}^* = f(z^*)$, and the above deformation cannot be applied. Therefore, we have

$$\frac{2C_F}{\pi r}\mathrm{Im}\int_{C_b}\frac{dq}{q}\left[iqr-\frac{i}{6}(qr)^3\right]\alpha_V(q^2)=\mathcal{C}_0(\mu_f)+\mathcal{C}_2(\mu_f)r^2\,, \tag{B.7}$$

where μ_f dependence remains.

Based on the above argument, we can construct a μ_f-independent quantity V_S^{RF}. Note that a μ_f-independent part is also given by the integral along C_a. Then by collecting all the μ_f-independent part, we obtain

$$V_S^{\mathrm{RF}}(r)=V_C(r)+\mathcal{C}_1 r \tag{B.8}$$

with

$$\begin{aligned}V_C(r)&=-\frac{1}{r}\left[\frac{2C_F}{\pi}\mathrm{Im}\int_{C_a}\frac{dq}{q}e^{iqr}\alpha_V(q^2)-\mathcal{C}_{-1}\right]\\&=-\frac{1}{r}\left[\frac{2C_F}{\pi}\int_0^\infty\frac{dq}{q}e^{-qr}\mathrm{Im}\,\alpha_V(-q^2+i0)-\mathcal{C}_{-1}\right].\end{aligned} \tag{B.9}$$

In the last line, we rotate the contour C_a to the line along $e^{i\pi/2}q$ with real positive q.

Once the μ_f-dependent part of $V_S(r;\mu_f)$ is considered as well, one obtains the decomposition shown in eq. (2.9).

C Definition of $\Lambda_{\overline{\mathrm{MS}}}$

The definition of the scale Λ in the $\overline{\mathrm{MS}}$ scheme, $\Lambda_{\overline{\mathrm{MS}}}$, is given by

$$\log\left(\frac{\mu^2}{\Lambda^2_{\overline{\mathrm{MS}}}}\right)=\frac{4\pi}{\alpha_s\beta_0}+\frac{\beta_1}{\beta_0^2}\log\left(\frac{\beta_0\alpha_s}{4\pi}\right)+\int_0^{\alpha_s}dx\left(\frac{1}{\beta(x)}+\frac{4\pi}{\beta_0x^2}-\frac{\beta_1}{\beta_0^2x}\right), \tag{C.1}$$

where α_s represents the coupling at the renormalization scale μ. We approximate the β function at four-loop as in eq. (2.8), which gives the definition of $\Lambda_{\overline{\mathrm{MS}}}^{\text{4-loop}}$, used extensively in this paper.

D χ^2 and covariance matrix

We present definitions of χ^2 and covariance matrices used in our analyses, which may be useful especially for non-expert readers.

Interpolation [analysis (I)]. We define χ^2 in the interpolation with a covariance matrix as[32]

$$\chi^2_{\mathrm{Inter}}(\alpha,c_0,\sigma,c_1,c_2)|_{d,i}=\sum_{k,l}[V_{\mathrm{latt},d,i}(r_k)-V^{\mathrm{Inter.}}_{\mathrm{latt},d,i}(r_k)]\Delta^{\mathrm{latt}}_{d,i}(r_k,r_l)^{-1}[V_{\mathrm{latt},d,i}(r_l)-V^{\mathrm{Inter.}}_{\mathrm{latt},d,i}(r_l)], \tag{D.1}$$

[32] χ^2 is a dimensionless quantity. Accordingly, each quantity appearing in eq. (D.1) can be made dimensionless. In practice, we normalize all the quantities with a.

JHEP04(2019)155

	0.7196	0.7822	1.043	1.079	1.304	1.439
0.7196	8.61×10^{-5}	-1.47×10^{-6}	-8.72×10^{-8}	1.79×10^{-6}	-5.14×10^{-6}	2.36×10^{-5}
0.7822		5.24×10^{-5}	9.45×10^{-7}	-1.76×10^{-7}	2.25×10^{-5}	-4.33×10^{-6}
1.043			2.18×10^{-8}	-3.54×10^{-9}	6.34×10^{-7}	-7.32×10^{-8}
1.079				1.07×10^{-7}	-1.25×10^{-7}	2.40×10^{-6}
1.304					2.27×10^{-5}	-1.65×10^{-6}
1.439						6.90×10^{-5}

Table 8. Covariance matrix for $X^{\rm cont}_{\rm latt}$, $\Delta^{\rm cont}(r_i, r_j)$. The first row is r_i/r_1 and the first column is r_j/r_1. The (i, j) component is the numerical value of $\Delta^{\rm cont}(r_i, r_j)$. Note that $\Delta^{\rm cont}(r_i, r_j)$ is a symmetric matrix, and hence, we only show the elements of the upper triangular part.

where $V^{\rm Inter.}_{{\rm latt},d,i}(r)$ is defined in eq. (3.2) and k, l run over the lattice points under consideration. The covariance matrix $\Delta^{\rm latt}(r_k, r_l)$ is calculated as

$$\Delta^{\rm latt}_i(r_k, r_l) = (N_i - 1)\left\langle (V_{{\rm latt},i}(r_k) - \langle V_{{\rm latt},i}(r_k)\rangle) \cdot (V_{{\rm latt},i}(r_l) - \langle V_{{\rm latt},i}(r_l)\rangle)\right\rangle \tag{D.2}$$

in the jackknife method, where N_i is the number of bins for the i-th lattice simulation; see table 1. If the subscript d is shown, it expresses a covariance matrix among the potentials $V_{{\rm latt},i,d}$.[33]

Continuum extrapolation [Analysis (I)]. χ^2 in the extrapolation to the continuum limit is defined as

$$\chi^2_{\rm ex}(\gamma, \delta; r) = \sum_{i=1,2,3} \left(\frac{X_{\rm latt}(r; a_i) - Y(a_i)}{\delta X_{\rm latt}(r; a_i)} \right)^2 , \tag{D.3}$$

where $Y(a)$ is defined by eq. (3.3).

The covariance matrix for $X^{\rm cont}_{\rm latt}$ is calculated as

$$\Delta^{\rm cont}(r_i, r_j) = (N_{\rm tot} - 1)\left\langle (X^{\rm cont}_{\rm latt}(r_i) - \langle X^{\rm cont}_{\rm latt}(r_i)\rangle) \cdot (X^{\rm cont}_{\rm latt}(r_j) - \langle X^{\rm cont}_{\rm latt}(r_j)\rangle)\right\rangle . \tag{D.4}$$

Note that in the continuum extrapolation, the jackknife samples with the size $N_{\rm tot} = \sum_{i=1}^{3} N_i = 400$ are generated since we have three independent lattice measurements. We present the numerical result of $\Delta^{\rm cont}$ in table 8.

Matching [Analysis (I)]. We define χ^2 in the matching of Analysis (I) as

$$\chi^2_{\rm match}(x, A_0, A_2) = \sum_{i,j} [\tilde{X}_{\rm latt}(r_i) - v_{\rm OPE}(r_i)] \tilde{\Delta}^{\rm cont}(r_i, r_j)^{-1} [\tilde{X}_{\rm latt}(r_j) - v_{\rm OPE}(r_j)] , \tag{D.5}$$

where $v_{\rm OPE}$ is given in eq. (3.6) and $\tilde{\Delta}^{\rm cont}$ is the covariance matrix for $\tilde{X}^{\rm cont}_{\rm latt}(r)$:

$$\tilde{\Delta}^{\rm cont}(r_i, r_j) = x^{-2} \Delta^{\rm cont}(r_i, r_j) . \tag{D.6}$$

See eq. (D.4) and table 8 for $\Delta^{\rm cont}$.

[33] Although in Analysis (I) we treat the data separately according to each direction, we will use them simultaneously in Analysis (II). This is the reason why we suppress the subscript d in eq. (D.2).

JHEP04(2019)155

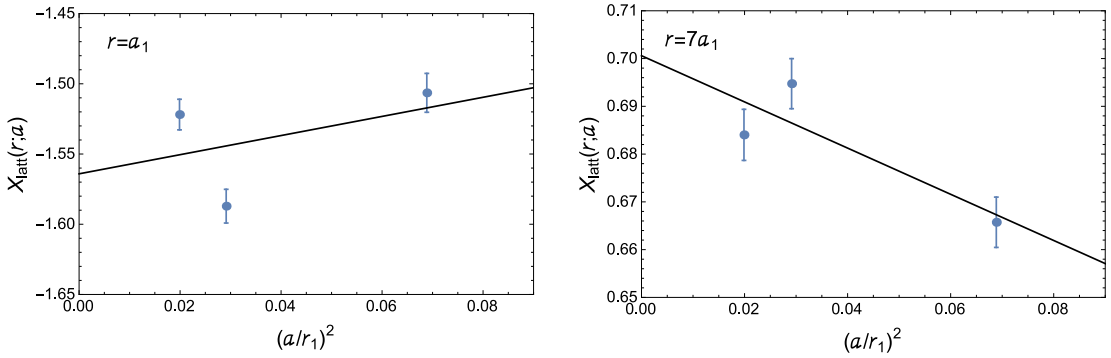

Figure 15. $X_{\rm latt}(r;a)$ as functions of $(a/r_1)^2$ when we include $r=a$ in interpolation. We show them for $r=a_1$ (left) and $r=7a_1$ (right), which are reference distances for $d=1$. Black lines are linear functions in a^2 determined by fits. $\chi^2_{\rm ex}$/d.o.f., which is the reduced χ^2 in this extrapolation, are 20 (left) and 4.3 (right).

Global fit [Analysis (II)]. We define χ^2 in the global fit in Analysis (II) as

$$\chi^2_{\rm GF}(z=\Lambda_{\overline{\rm MS}},A_2,\kappa,f,c_0)=\sum_{i,j}[V^{\rm cont}_{\rm latt}(r_i)-V_{\rm OPE}(r_i)]\Delta^{\rm latt}(r_i,r_j)^{-1}[V^{\rm cont}_{\rm latt}(r_j)-V_{\rm OPE}(r_j)]\,. \tag{D.7}$$

Here, the covariance matrix consists of three matrices of dimension 7, 10, and 13 in a block diagonal form:

$$\Delta^{\rm latt}=\begin{pmatrix}\Delta^{\rm latt}_1 & O & O\\ O & \Delta^{\rm latt}_2 & O\\ O & O & \Delta^{\rm latt}_3\end{pmatrix}\,, \tag{D.8}$$

where the definition of each matrix is given by eq. (D.2).

E Case including data at $r=a$ in Analysis (I)

In Analysis (I), we do not use the data at $r=a$ in interpolating lattice data in our analyses, in order to suppress serious finite a effects. Here, let us see what happens if we include this shortest point. We interpolate lattice data including the ones at $r=a$, and obtain $X_{\rm latt}(r;a)$ in the same way. In figure 15, we plot the data points of $X_{\rm latt}(r;a)$ taking the horizontal axis as $(a/r_1)^2$. One can see that they do not obey linear behaviors in a^2. We remark that even the data for $r=7a_1$, where the finite a effect is considered to be well suppressed, cannot smoothly be extrapolated to the continuum limit. It shows that the data at $r=a$, which has a small statistical error, dominantly contributes to determining the interpolating function, and thus, the interpolating function is seriously distorted. In figure 16, we show $\chi^2_{\rm ex}$/d.o.f. in this case, corresponding to figure 5. Extrapolations to the continuum limit do not work for $d=1$. For $d=2$, where the shortest point is located at $r=\sqrt{2}a$, extrapolations work better than for $d=1$. We conclude that the data at $r=a$ has serious discretization error, and we should be cautious about treating it.

JHEP04(2019)155

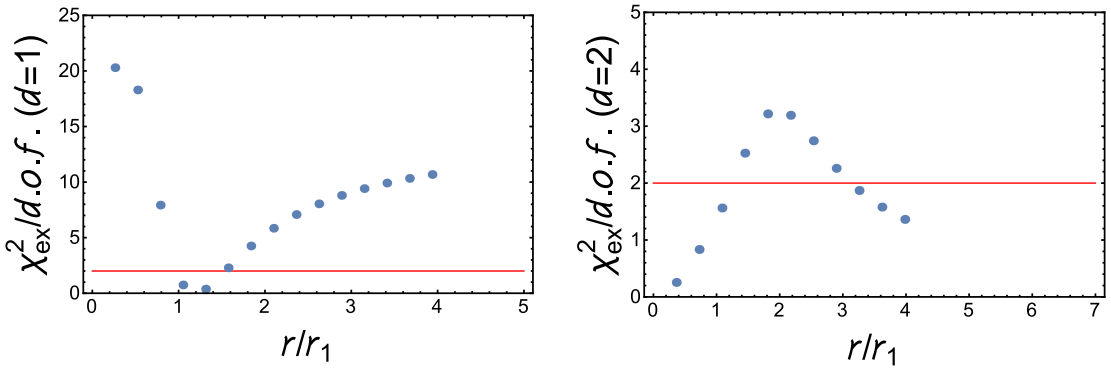

Figure 16. The reduced $\chi^2_{\rm ex}$ in extrapolations. $\chi^2_{\rm ex}/{\rm d.o.f.} = 2$ is shown by red lines as a benchmark.

F Additional analyses on systematic errors

In this appendix, we provide supplemental analyses to check validity of our error analyses from additional aspects.

$\mathcal{O}(a^4)$ effect. In section 3, we considered the leading discretization error, the quadratic effect in a, of the lattice data. Here, we estimate the possible effect coming from the neglected $\mathcal{O}(a^4)$ error.[34]

In both Analyses (I) and (II), if we perform fits including $\mathcal{O}(a^4)$ terms it turns out that the fits have little sensitivities to these terms, given the current lattice data. As a result, the fits become fairly unstable, leading to fairly uncertain results for $\alpha_s(M_Z^2)$ [even though they are consistent with eqs. (3.8) and (3.19) within estimated (large) errors].

Instead we can confirm that our analysis is stable against possible $\mathcal{O}(a^4)$ effects in the following way in the case of Analysis (II). We add an $\mathcal{O}(a^4)$-term to eq. (3.16) as $g_d a_i^4/r^5$ while fixing g_d. In this analysis, to properly consider the expansion in a/r up to NLO, we omit the data at $r < 2a$ because this expansion is not legitimate when the data at $r = a$ is included, as clarified in appendix E. In this case, the tree-level correction is not necessary and is omitted (see footnote 27). To assume a reasonable size of g_d, we refer to the size of f_d, the coefficients of the $\mathcal{O}(a^2)$ error, determined from the data at $r \geq 2a$. They read $f_1 = 0.04, f_2 = -0.008$. Then, we assume $g_1 = g_2 = 0.04t$ and vary $t = -1$ to $+1$. The other parameters (such as f_d and $\Lambda_{\overline{\rm MS}}$) are treated as fitting parameters. The largest variation of α_s caused by the $\mathcal{O}(a^4)$-term is obtained as $\Delta\alpha_s(M_Z^2) = -0.0003$. This is comparable to the assigned error in table 7 in Analysis (II). This result indicates that our error analysis concerning finite a effects is reasonable even if we take into account the neglected higher order discretization errors.

Mass correction. In section 3.3, the effect of the mass deviation in the lattice simulations was estimated based on perturbation theory, where it was found negligibly small. We support this result by directly comparing lattice results with different pion masses. We analyze the lattice data with $M_\pi = 300$ and 408 MeV for the lattice spacing a_2 [25]. (Here,

[34] Due to chiral symmetry, an $\mathcal{O}(a^3)$ error is prohibited.

JHEP04(2019)155

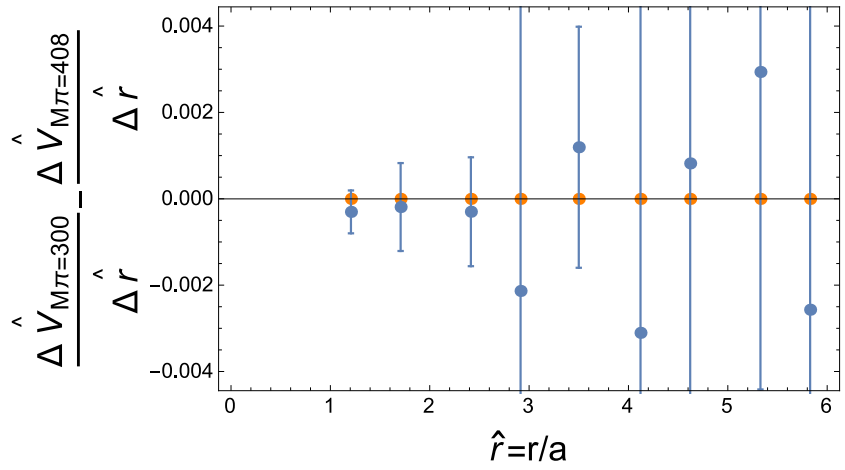

Figure 17. Difference of the (approximate) slopes of the potentials in the different pion masses ($M_\pi = 300\,\mathrm{MeV}$ and $408\,\mathrm{MeV}$). The potential V and distance r are normalized by lattice spacing a. The blue data show the lattice results with statistical errors. The orange points are the perturbative estimate.

t	-0.3	-0.1	0.1	0.3
A_2 [GeV^3]	-0.01	-0.01	-0.008	-0.007
$\Delta\alpha_s(M_Z^2)\times 10^4$	2	1	-0	-1

Table 9. Values of A_2 and variation of $\alpha_s(M_Z^2)$ when the logarithmic correction of eq. (F.1) is considered.

we neglect finite a effects.) Since the slope of the potential affects α_s, we examine the *difference* of the slopes. The slopes are approximately obtained from the difference of the potentials at the nearest neighbor. In figure 17, the difference of the (approximate) slopes is shown, where it is consistent with zero.[35] (In Analysis (II), we use the first 10 points.) This result is consistent with our error estimate that the mass effect is negligibly small.

Possible logarithmic correction to r^2-term. We have treated the nonperturbative effect as $\delta E_{\mathrm{US}}^{\mathrm{RF}}(r) = A_2 r^2$. There is a possibility that this r^2-term is modified by logarithmic corrections, which may stem from higher order computations of Wilson coefficients. Here, we examine how large such a logarithmic correction affects our α_s determination.

In Analysis (II), we assume $\delta E_{\mathrm{US}}^{\mathrm{RF}}(r)$ as

$$\delta E_{\mathrm{US}}^{\mathrm{RF}}(r) = A_2\left[1 + t\log\left(r\cdot 1\ \mathrm{GeV}\right)\right] r^2 \tag{F.1}$$

with $t = -0.3, -0.1, 0.1, 0.3$. Then, we obtain the result in table 9. (We also use $1.5\,\mathrm{GeV}$ and $0.5\,\mathrm{GeV}$ instead of $1\,\mathrm{GeV}$ as a scale in the logarithm. We find that the results hardly change.) One sees that this uncertainty dose not induce a dominant systematic error, and thus, is not included in our final result.

[35] The slope itself (before taking the difference) is about 0.1 in the same units.

JHEP04(2019)155

Open Access. This article is distributed under the terms of the Creative Commons Attribution License (CC-BY 4.0), which permits any use, distribution and reproduction in any medium, provided the original author(s) and source are credited.

References

[1] Particle Data Group collaboration, *Review of Particle Physics*, *Chin. Phys.* **C 40** (2016) 100001 [INSPIRE].

[2] S. Aoki et al., *Review of lattice results concerning low-energy particle physics*, *Eur. Phys. J.* **C 77** (2017) 112 [arXiv:1607.00299] [INSPIRE].

[3] K. Maltman, D. Leinweber, P. Moran and A. Sternbeck, *The Realistic Lattice Determination of $\alpha_s(M_Z)$ Revisited*, *Phys. Rev.* **D 78** (2008) 114504 [arXiv:0807.2020] [INSPIRE].

[4] PACS-CS collaboration, *Precise determination of the strong coupling constant in $N_f = 2+1$ lattice QCD with the Schrödinger functional scheme*, *JHEP* **10** (2009) 053 [arXiv:0906.3906] [INSPIRE].

[5] C. McNeile, C.T.H. Davies, E. Follana, K. Hornbostel and G.P. Lepage, *High-Precision c and b Masses and QCD Coupling from Current-Current Correlators in Lattice and Continuum QCD*, *Phys. Rev.* **D 82** (2010) 034512 [arXiv:1004.4285] [INSPIRE].

[6] B. Chakraborty et al., *High-precision quark masses and QCD coupling from $n_f = 4$ lattice QCD*, *Phys. Rev.* **D 91** (2015) 054508 [arXiv:1408.4169] [INSPIRE].

[7] A. Bazavov, N. Brambilla, X. Garcia i Tormo, P. Petreczky, J. Soto and A. Vairo, *Determination of α_s from the QCD static energy: An update*, *Phys. Rev.* **D 90** (2014) 074038 [arXiv:1407.8437] [INSPIRE].

[8] M. Lüscher, P. Weisz and U. Wolff, *A numerical method to compute the running coupling in asymptotically free theories*, *Nucl. Phys.* **B 359** (1991) 221 [INSPIRE].

[9] M. Lüscher, R. Narayanan, P. Weisz and U. Wolff, *The Schrödinger functional: A renormalizable probe for nonAbelian gauge theories*, *Nucl. Phys.* **B 384** (1992) 168 [hep-lat/9207009] [INSPIRE].

[10] M. Lüscher, R. Sommer, P. Weisz and U. Wolff, *A precise determination of the running coupling in the* SU(3) *Yang-Mills theory*, *Nucl. Phys.* **B 413** (1994) 481 [hep-lat/9309005] [INSPIRE].

[11] S. Sint, *On the Schrödinger functional in QCD*, *Nucl. Phys.* **B 421** (1994) 135 [hep-lat/9312079] [INSPIRE].

[12] ALPHA collaboration, *QCD Coupling from a Nonperturbative Determination of the Three-Flavor Λ Parameter*, *Phys. Rev. Lett.* **119** (2017) 102001 [arXiv:1706.03821] [INSPIRE].

[13] M. Beneke, *Renormalons*, *Phys. Rept.* **317** (1999) 1 [hep-ph/9807443] [INSPIRE].

[14] A.H. Mueller, *On the Structure of Infrared Renormalons in Physical Processes at High-Energies*, *Nucl. Phys.* **B 250** (1985) 327 [INSPIRE].

[15] Y. Sumino, *Static QCD potential at $r < \Lambda_{\rm QCD}^{-1}$: Perturbative expansion and operator-product expansion*, *Phys. Rev.* **D 76** (2007) 114009 [hep-ph/0505034] [INSPIRE].

JHEP04(2019)155

[16] G. Mishima, Y. Sumino and H. Takaura, *Subtracting infrared renormalons from Wilson coefficients: Uniqueness and power dependences on $\Lambda_{\rm QCD}$*, *Phys. Rev.* **D 95** (2017) 114016 [arXiv:1612.08711] [INSPIRE].

[17] M. Beneke, *A quark mass definition adequate for threshold problems*, *Phys. Lett.* **B 434** (1998) 115 [hep-ph/9804241] [INSPIRE].

[18] A.H. Hoang, M.C. Smith, T. Stelzer and S. Willenbrock, *Quarkonia and the pole mass*, *Phys. Rev.* **D 59** (1999) 114014 [hep-ph/9804227] [INSPIRE].

[19] N. Brambilla, A. Pineda, J. Soto and A. Vairo, *Potential NRQCD: An effective theory for heavy quarkonium*, *Nucl. Phys.* **B 566** (2000) 275 [hep-ph/9907240] [INSPIRE].

[20] A.V. Smirnov, V.A. Smirnov and M. Steinhauser, *Fermionic contributions to the three-loop static potential*, *Phys. Lett.* **B 668** (2008) 293 [arXiv:0809.1927] [INSPIRE].

[21] C. Anzai, Y. Kiyo and Y. Sumino, *Static QCD potential at three-loop order*, *Phys. Rev. Lett.* **104** (2010) 112003 [arXiv:0911.4335] [INSPIRE].

[22] A.V. Smirnov, V.A. Smirnov and M. Steinhauser, *Three-loop static potential*, *Phys. Rev. Lett.* **104** (2010) 112002 [arXiv:0911.4742] [INSPIRE].

[23] R.N. Lee, A.V. Smirnov, V.A. Smirnov and M. Steinhauser, *Analytic three-loop static potential*, *Phys. Rev.* **D 94** (2016) 054029 [arXiv:1608.02603] [INSPIRE].

[24] JLQCD collaboration, *Large-scale simulations with chiral symmetry*, PoS(LATTICE 2013)125 [arXiv:1311.6941] [INSPIRE].

[25] JLQCD collaboration, in preparation.

[26] F. Karbstein, M. Wagner and M. Weber, *Determination of $\Lambda_{\overline{MS}}^{(n_f=2)}$ and analytic parameterization of the static quark-antiquark potential*, *Phys. Rev.* **D 98** (2018) 114506 [arXiv:1804.10909] [INSPIRE].

[27] H. Takaura, T. Kaneko, Y. Kiyo and Y. Sumino, *Determination of α_s from static QCD potential with renormalon subtraction*, *Phys. Lett.* **B 789** (2019) 598 [arXiv:1808.01632] [INSPIRE].

[28] H. Takaura, *Renormalon free part of an ultrasoft correction to the static QCD potential*, *Phys. Lett.* **B 783** (2018) 350 [arXiv:1712.05435] [INSPIRE].

[29] T. Appelquist, M. Dine and I.J. Muzinich, *The Static Potential in Quantum Chromodynamics*, *Phys. Lett.* **69B** (1977) 231 [INSPIRE].

[30] N. Brambilla, A. Pineda, J. Soto and A. Vairo, *The infrared behavior of the static potential in perturbative QCD*, *Phys. Rev.* **D 60** (1999) 091502 [hep-ph/9903355] [INSPIRE].

[31] P. Weisz, *Continuum Limit Improved Lattice Action for Pure Yang-Mills Theory. 1.*, *Nucl. Phys.* **B 212** (1983) 1 [INSPIRE].

[32] R.C. Brower, H. Neff and K. Orginos, *The Möbius domain wall fermion algorithm*, *Comput. Phys. Commun.* **220** (2017) 1 [arXiv:1206.5214] [INSPIRE].

[33] M. Lüscher, *Properties and uses of the Wilson flow in lattice QCD*, *JHEP* **08** (2010) 071 [*Erratum ibid.* **03** (2014) 092] [arXiv:1006.4518] [INSPIRE].

[34] JLQCD collaboration, *Renormalization of domain-wall bilinear operators with short-distance current correlators*, *Phys. Rev.* **D 94** (2016) 054504 [arXiv:1604.08702] [INSPIRE].

JHEP04(2019)155

[35] G.S. Bali and K. Schilling, *Static quark-anti-quark potential: Scaling behavior and finite size effects in* SU(3) *lattice gauge theory*, *Phys. Rev.* **D 46** (1992) 2636 [INSPIRE].

[36] MILC collaboration, *Results for light pseudoscalar mesons*, PoS(LATTICE 2010)074 (2010) [arXiv:1012.0868] [INSPIRE].

[37] A. Bazavov et al., *The chiral and deconfinement aspects of the QCD transition*, *Phys. Rev.* **D 85** (2012) 054503 [arXiv:1111.1710] [INSPIRE].

[38] R. Sommer, *Scale setting in lattice QCD*, PoS(LATTICE 2013)015 (2014) [arXiv:1401.3270] [INSPIRE].

[39] Y. Sumino, *Understanding Interquark Force and Quark Masses in Perturbative QCD*, arXiv:1411.7853 [INSPIRE].

[40] K.G. Chetyrkin, B.A. Kniehl and M. Steinhauser, *Strong coupling constant with flavor thresholds at four loops in the MS scheme*, *Phys. Rev. Lett.* **79** (1997) 2184 [hep-ph/9706430] [INSPIRE].

[41] A.H. Hoang, *Bottom quark mass from Upsilon mesons: Charm mass effects*, hep-ph/0008102 [INSPIRE].

[42] M. Melles, *The static QCD potential in coordinate space with quark masses through two loops*, *Phys. Rev.* **D 62** (2000) 074019 [hep-ph/0001295] [INSPIRE].

[43] S. Recksiegel and Y. Sumino, *Perturbative QCD potential, renormalon cancellation and phenomenological potentials*, *Phys. Rev.* **D 65** (2002) 054018 [hep-ph/0109122] [INSPIRE].

[44] S. Borsányi et al., *High-precision scale setting in lattice QCD*, *JHEP* **09** (2012) 010 [arXiv:1203.4469] [INSPIRE].

JHEP04(2019)155